Spatio–Temporal Patterns, Correlations, and Disorder in Evolutionary Game Theory

Qian He

Dissertation submitted to the Faculty of the
Virginia Polytechnic Institute and State University
in partial fulfillment of the requirements for the degree of

Doctor of Philosophy
in
Physics

Uwe C. Täuber, Chair
Michel J. Pleimling
Jean J. Heremans
Kyungwha Park

November 7, 2011
Blacksburg, Virginia

Keywords: evolutionary game theory, rock-paper-scissors game, correlation, spatial disorder, universal scaling in financial market, heterogeneity, Monte Carlo simulation.

Spatio–Temporal Patterns, Correlations, and Disorder in Evolutionary Game Theory

(Abstract)

Evolutionary game theory originated from the application of mathematical game theory to biological studies. Well-known examples in evolutionary game theory are the prisoner's dilemma, predator-prey models, the rock-paper-scissors game, etc. Recently, such well-known models have attracted increased interest in population dynamics to understand the emergence of biodiversity and species coexistence. Meanwhile, it has been realized that techniques from statistical physics can aid us to gain novel insights into this interdisciplinary field. In our research, we mainly employ individual-based Monte Carlo simulations to study emerging spatio-temporal patterns, spatial correlations, and the influence of quenched spatial disorder in rock-paper-scissors systems either with or without conserved total population number. In balanced rock-paper-scissors systems far away from the "corner" of configuration space, it is shown that quenched spatial disorder in the reaction rates has only minor effects on the co-evolutionary dynamics. However, in model variants with strongly asymmetric rates (i.e., "corner" rock-paper-scissors systems), we find that spatial rate variability can greatly enhance the fitness of both minor species in"corner" systems, a phenomenon already observed in two-species Lotka-Volterra predator-prey models. Moreover, we numerically study the influence of either pure hopping processes or exchange processes on the emergence of spiral patterns in spatial rock-paper-scissors systems without conservation law (i.e., May-Leonard model). We also observe distinct extinction features for small spatial May-Leonard systems when the mobility rate crosses the critical threshold which separates the active coexistence state from an inactive absorbing state.

In addition, through Monte Carlo simulation on a heterogeneous interacting agents model, we investigate the universal scaling properties in financial markets such as the fat-tail distributions in return and trading volume, the volatility clustering, and the long-range correlation in volatility. It is demonstrated that the long-tail feature in trading volume distribution results in the fat-tail distribution of asset return, and furthermore it is shown that the long tail in trading volume distribution is caused by the heterogeneity in traders' sensitivities to market risk.

This work is in part supported by Virginia Tech's Institute for Critical Technology and Applied Science (ICTAS) through a Doctoral Scholarship.

Dedication

To my parents Dacai He and Wanfen Zhang, my sister Chunrong He, and my brother Tao Zhang

Acknowledgements

First of all, let me take this opportunity to thank my supervisor Dr. Uwe Täuber for his professional guidance and persistent support throughout my Ph.D. study. Without his support, it would be impossible for me to accomplish my Ph.D. work and my simultaneous Master degree in Applied Economics. His rigorous standards on my work aid me to achieve a quality of preciseness on scientific research. I believe this precious quality will benefit my future life and career development in the long run. Uwe also helped me refine my English language skills, guided me to write and speak as a scientific researcher, and encouraged me to enjoy every day in my Ph.D. life. I appreciate his help and patience during the past four years, and I am really glad to have him as my Ph.D. advisor.

I would like to thank my committee members: Dr. Michel Pleimling, Dr. Jean Heremans and Dr. Kyungwha Park . I really appreciate their time spent on reading and commenting my dissertation. My Ph.D. study is in part supported by ICTAS scholarship. Many thanks to Dr. Roop Mahajan and Mrs Ann Craig in ICTAS for their help and support.

I would like to acknowledge Dr. Mauro Mobilia for the collaboration in our research projects. My dissertation includes his contribution in the projects, I am very glad to collaborate with him and many thanks for his effort.

I would also like to thank all my friends in Blacksburg. They are always there to support anytime when I need them, and they make my life in USA wonderful. I especially acknowledge Dr. Sven Dorosz, Ulrich Dobramysl, Dr. George Daquila, and Yoh Yamamoto for the joy in the office, I am really glad that we worked together during the past several years.

Finally, my special thanks to my parents and my dearest sister and brother. Their love and support always cheer me up and make me succeed in reaching my goals. I love them for ever, and I wish them health and happiness every day.

Contents

List of Figures

List of Tables

Chapter 1

Introduction

Evolutionary game theory is an application of mathematical game theory to biological context. It was first developed in 1930 by R. A. Fisher in his book "The Genetic Theory of Natural Selection", in which he was trying to explain the puzzle of approximate equality of sex ratio in many species where the majority of males never mate [1]. Fisher discovered that if we define the fitness of one individual as the expected average number of its grandchildren, then individual fitness is determined by the relative ratio of males to females in the species, and further such evolving fluctuating ratios result in the approximate equality of sex ratio in species systems. In fact, such relative population ratio introduces a strategy element of game theory into the population systems. In 1972, the concept of stable strategy in evolutionary game theory was defined by Maynard Smith, and the publication of his work "Evolution and the Theory of Games" in 1982 more systematically presented the evolutionary game theory and its applications in biological studies. Since then, evolutionary game theory has been attracting persistent attention in biology, economics, and social science.

Compared with classical game theory in mathematics, evolutionary game theory focuses more on the dynamics in modeling biological/social systems. Therefore, when employing evolutionary game theory to analyze biological/social systems, there are two main approaches to the associated evolutionary games. The first one is the tool of stable strategy in game theory, but this tool is static and it does not refer to the underlying dynamic processes on how to reach the stable strategies (assuming such stable strategies exist). In contrast, the second approach does not aim at the stable strategies but at the underlying evolving dynamic processes by explicitly specifying the system models. Meanwhile, as observed in many physical systems in statistical physics, population systems usually consist of a large number of interacting individuals/particles. Therefore, once the explicit models are specified, we can employ the techniques from statistical physics to analyze the emergence of fluctuations, correlations, and complex spatio-temporal patterns in the population evolution, aiding us to gain novel insights into evolutionary game theory in population dynamics. From Chapter 2 to Chapter 4, we shall employ mean-field theory and Monte Carlo simulations to investigate several

model variants of well-known games such as the rock–paper–scissors game and predator–prey models. Particularly, in Chapter 2, we are going to study the rock–paper–scissors game with conserved total population number; in Chapter 3, we shall turn to the rock–paper–scissors model without the conservation law (i.e., May–Leonard model); furthermore, the connection between the rock–paper–scissors model and Lotka–Volterrra predator-prey model is studied in Chapter 4. In Chapter 5, we shall employ an interacting agents model to study the emergence of universal scaling properties in financial markets.

The introduction content about evolutionary game theory either has been published in the references [2, 3] or is in preparation for publication [4]. Understanding the origin of and maintaining biodiversity is of obvious paramount importance in ecology and biology [5, 6, 7, 8, 9]. In this context, paradigmatic schematic models of predator–prey interaction that build on the classic Lotka–Volterra system [10, 11] have been widely studied. Specifically, systems with cyclic dominance of competing populations have been suggested to provide a mechanism to promote species diversity; there are also natural connections to evolutionary game theory [12, 13, 14, 15, 16, 17]. A minimal yet non-trivial model for cyclic competition is the three-species cyclic predator–prey system with standard Lotka–Volterra predation interactions, essentially equivalent to the familiar rock–paper–scissors (RPS) game [12, 13, 14, 15]. This RPS system has, for example, been used to model the cyclic competitions between three subspecies of certain Californian lizards [18, 19], and the coevolution of three strains of *E. coli* bacteria in microbial experiments [20]. Other examples include coral reef invertebrates [21] and overgrowths by marine sessile organisms [22, 23]. In this simple RPS model, one lets 'rock' (species A) smash 'scissors' (species B), 'scissors' cut 'paper' (species C), and 'paper' wrap 'rock'. Already for a non-spatial RPS system, the presence of intrinsic stochastic fluctuations (reaction noise) makes the system eventually evolve to one of the three extinction states where only one species survives [24, 25, 26, 27]. For example, if the reaction rates in the system are not equal, one intriguingly observes the 'weakest' species, with the smallest predation rate, to survive, whereas the other two species always die out [26, 27]. When the model is extended to include spatial degrees of freedom, e.g., by allowing particles to hop to nearest-neighbor sites on a lattice and interact upon encounter, spatial fluctuations and correlations further complicate the picture. For instance, species extinction still prevails in one-dimensional RPS models [28, 29, 30, 31], but the system settles in a coexistence state when the species are efficiently mixed through particle exchange (see Ref. [32]). In contrast, two-dimensional RPS systems are characterized by coexistence of the competing species, and the emergence of complex spatio-temporal structures such as spiral patterns [26, 28, 31, 33, 34, 35, 36, 37, 38, 39, 40, 41, 42]. Recently, as one of various RPS variants, the four-state RPS model without conservation law (i.e., May–Leonard model) has received much attention [37, 38, 39, 40, 42]; it is now well-established that cyclic reactions in conjunction with diffusive spreading generate spiral patterns (when the system is sufficiently mixed), leading to novel results that have important implications for the formation and propagation of spatial patterns in ecological systems. In model variants that incorporate conservation of the total population density, on the other hand, spiral patterns do not occur [26, 28, 42]; also, when the species mobility is drastically enhanced through fast particle exchange processes,

the spiral patterns are destroyed as well, and the system eventually reaches an extinction state [37, 42].

Coexistence and competition of biological species are often crucially affected by environmental influences which include limited and randomly distributed natural resources, the availability of shelter, varying climate conditions, etc. Our work is motivated by the following question: Which are the crucial model ingredients to be included in order to attain a further degree of realism? Therefore, it is important to understand the precise role of limited carrying capacity and spatial inhomogeneity on the formation and development of biodiversity. Naturally, lattice models should be viewed as coarse-grained representations of a metapopulation system where each lattice site or cell can be interpreted as a 'patch' (or 'island') populated by a 'deme' (or 'local community') [43, 44]. For the sake of simplicity (i.e. to try to understand the simplest possible systems before venturing further), we restrict our presentation in Chapter 2 to RPS model variants that obey a conservation law (even though that has no particular ecological motivation). As empty lattice sites are allowed, we shall refer to our model system in Chapter 2 as a class of four-state RPS models with conservation law (if all sites are at most occupied by a single individual, each of them can be in one of four states) where the total population size is conserved (zero-sum games) [13, 15, 24, 26, 28, 29, 30, 31, 33, 34, 37, 41, 42, 45]. However, in Chapter 3 we shall turn to the RPS model variants without the conservation of the total number of particles (i.e., May–Leonard model), where spiral waves emerge in RPS systems.

In our stochastic lattice models, the carrying capacity (i.e., the maximum population size that can be sustained by the environment) is implemented through site occupation number restrictions. Environmental variability for the RPS systems with conservation law in Chapter 2 is modeled through assigning local reaction rates that are treated as quenched random variables drawn from a uniform distribution, while in Chapter 3 we model the environmental variability in May–Leonard model by implementing the reaction (and mobility) rates as quenched random variables that for each lattice site are independently drawn from a truncated Gaussian distribution. Our extensive numerical study in Chapter 2 shows that carrying capacity and quenched disorder have little influence on the oscillatory dynamics, spatial correlation functions, and extinction times in the RPS model systems with conservation law. Furthermore, the effects (or lack thereof) of limited carrying capacity and random environmental influences on the transient population oscillations, spatial correlation functions, and species extinction times are common to models without conservation laws (i.e., May–Leonard model) [2]. This demonstrates a quite remarkable robustness of this class of models. From a modeling perspective, this establishes the essential equivalence of rather distinct model variants. We emphasize that this outcome is nontrivial, as is, for example, revealed by a comparison with the two-species Lotka-Volterra system [46, 47], where spatially varying reaction rates may cause more localized clusters of activity and thereby enhance the fitness of both predator and prey species [48].

For two-dimensional version of May–Leonard model, in addition the self-organization of the population and spatio-temporal correlation functions in the coexistence phase, we also

explore the statistics of species extinction times (for small system sizes). Our main results for May–Leonard model in Chapter 3 can be summarized as follows:

(1) We demonstrate that quenched spatial disorder has only minor effect on species coexistence in the May-Leonard model, which together with the results reported in Chapter 2, shows that RPS models (in the presence or absence of total particle number conservation) form a class of systems that are robust against environmental variability. Remarkably, this statement is true even when spatial disorder affects the particles' mobility which is known to drastically impact species coexistence.

(2) We study the combined effect of pair exchange and hopping processes in two-dimensional May–Leonard model, and demonstrate that the former are more important for the formation of robust spiral wave structures.

(3) We compute the extinction times, defined as the time when the first one of three species dies out, in (small) spatially extended May–Leonard systems. We thus find that the mean extinction time (MET) increases sharply with system size N when the mobility rate is low and the system is in the (long-lived metastable) coexistence state. However, once the mobility exceeds the threshold beyond which species extinction is prevalent, the MET function switches to a linear dependence on N. Correspondingly, the extinction time distribution is found to cross over from approximately exponential with prominent tail at large times, to a bell-shaped near-Gaussian function.

Understanding the connection between two-species LV model and three-species interacting models can provide some insights on reducing complex multi-species interacting systems to effective models with fewer degrees of freedom. In Chapter 4, we turn to carefully explore the relationship between both cyclic and hierarchical three-species predator prey systems and the two-species LV model (in preparation for publication [4]). The classic LV model captures the dynamical evolution of two competing species of predators and prey; in the well-mixed mean-field limit, the ensuing coupled deterministic nonlinear ordinary differential equations yield regular periodic population oscillations. However, this original non-spatial LV model is often criticized for its oversimplification [9] and lack of robustness: it is mathematically unstable against various model modifications and variations [49]. Therefore, hopefully more realistic stochastic spatial LV model extensions have been studied extensively both analytically and computationally; this includes the stochastic lattice-based LV model with unrestricted site occupancies [47, 48] and model versions with restricted local carrying capacity, where only a limited number of individuals may occupy each lattice site [46, 50, 51, 52, 53, 54]. Systems with restricted site occupancy have been shown to display a critical extinction threshold for the predator population, where in the thermodynamic limit a continuous phase transition takes place from an active coexistence state to an inactive absorbing state, governed by the power laws of critical directed percolation [46, 50, 51, 52, 53, 54, 55, 56, 57]. In the active (quasi-)stationary coexistence state, stochastic spatial LV models display essential and robust features such as species clustering and the emergence of correlated spreading activity fronts [46, 47, 52, 53, 58, 59, 60, 61, 62], the presence of persistent characteristic

erratic population oscillations [31, 46, 47, 51, 52, 53, 54, 57, 63], and fitness enhancement for both species induced by significant spatial variability in the predation rates that control the interactions between predators and prey [48].

In the three-species cyclic RPS model, when one of the three species possesses a persistent large population density $O(1)$ in (quasi-)steady state (i.e., majority species) and meanwhile the other two species only have small population densities $O(1/N)$ (i.e., minority species), through treating the majority species in the system as empty states in spatial two-species LV system, the predation processes between the majority species and other two minority species in such "corner" RPS system can be rewritten as the elimination process of predator and reproduction process of prey in two-species LV model. That is, the evolutionary dynamics of the two minority species in the "corner" RPS model can be approximated by the two-species LV model, and the error limit of such approximation has been proved to be $O(1/N^2)$ [64]. Here N represents the typical size of living space for species (in lattice-based simulation, N is the typical size of lattice). Another example of three-species interacting models is the hierarchical three-species "food chain" system, which is generated by inserting one intermediate species between predator and prey in two-species LV model; then the predations between predator and prey are indirectly realized by the interactions between predator/prey and the intermediate species. Therefore, it is worth studying whether we can still use the two-species LV system, which has less reaction noise and lower degrees of freedom, to approximate the dynamic behavior of predator and prey in such three-species "food chain" systems.

Our main results in Chapter 4 can be summarized as follows:

(1) We demonstrate that the two minority species in three-species "corner" RPS system exhibit the similar evolutionary dynamics as the predator and prey in two-species LV system: quantitatively similar population densities in (quasi-)steady state, remarkable species clustering, and robust fitness enhancement due to spatial variability in predation rate (i.e., larger population densities for predator and prey in (quasi-)steady state, shorter relaxation time towards stationary coexisting state, and more localized species clusters), this result of fitness enhancement in "corner" RPS systems resemble the previous research result that quenched spatial disorder can greatly enhance the fitness of both predator and prey in two-species LV model [48]. Therefore, together with the mean-field analysis on the models, the numerical results confirm the first thought that two-species LV models can well approximate the evolutionary dynamics of the two minority species in three-species "corner" RPS model.

(2) We study the hierarchical three-species "food chain" model. In the spatially well-mixed version of such "food chain" model, there exists an extinction threshold as observed in two-species LV model with site restriction, and the numerical simulation results for coexistence states of the well-mixed systems are closely consistent with the predictions from mean-field theory. Meanwhile, we find that nearest-neighbor particle pair exchange processes alone are strong enough to wash out the emergence of species clusters, promote the appearance of mean-field like behavior, and eliminate the influence of quenched spatial disorder; while the spatial "food chain" system extended only through pure hopping processes does not

behave according to the mean-field predictions, and remarkable species clusters emerge in the system as observed in two-species LV systems. However, due to the interruption of intermediate species clusters, the effective reaction boundaries between predator clusters and prey clusters in such non well-mixed system are strongly suppressed, and correspondingly the spatial disorder in predation rate still does not have a robust influence on the evolutionary dynamics of the predator and prey in the "food chain" systems extended only through pure hopping processes. That is, the predator and prey in the hierarchical three-species "food chain" model do not behave like the predator and prey in two-species LV model.

The techniques from statistical physics can be applied not only to evolutionary game theory and population dynamics but also to social systems such as financial markets. In chapter 5, we employ an interacting agents model and study the universal scaling properties in financial markets (the model and its associated results presented in Chapter 5 have been studied and published in Ref. [65]). In the main economic theories, the assumption of efficient market hypothesis is the foundation for various asset pricing methods [66]. In the efficient market, one rational individual investor cannot consistently or persistently perform better/worse than the market index (such as S&P 500 and Nasdaq Composite), i.e., the investor should achieve the same risk-adjusted (i.e., normalized) return as market return on average. Particularly, on the ground of the strong efficient market hypothesis, the market price of one single asset stochastically fluctuates around the true underlying value of the asset, which is the time-adjusted sum of all expected future dividend payments for the asset. Then, the return should behave like a random walk, thus the variance of returns is going to be proportional to the duration of return horizon. However, the empirical data from the real market show that the time series of asset prices exhibit a remarkable property of mean-reverting [67], implying that there exists a strong correlation for price variations, a correlation which should not occur under the hypothesis of efficient market. Moreover, the empirical data show some other universal statistical properties characterizing various asset markets. These properties include fat-tail distribution of asset return [68, 69] and volatility clustering characterized by intermittent bursts of striking fluctuations [70]. Meanwhile, all those phenomena appear under the situation that the financial system consists of large amount of individual components (investors/agents). Then, it becomes quite intriguing how the complex micro-interactions between individual components pushes the emergence of such universal properties in the market. Therefore, to understand these universal properties in the market, various interacting agent models have been developed to mimic the dynamical behavior in one single asset market [65, 71, 72].

In statistical physics, the observed universal behavior is usually attributed to the explicit interactions between individual components in the models. However, it is also possible to extract complex universal behavior by indirect interaction between agents. The financial market is just such an example, i.e., while the agents/investors are independent from each other, they receive the same information from the financial market and further react to the information according to both their individual sensitivity to the market information and their expectation on the future market performance. Therefore, such information plays

an important role as a mean-field global variable to influence and mediate the individual agents/investors. Obviously, the asset price listed in the market is one of the most significant pieces of information to all investors, and naturally it becomes the appropriate global variable to couple the behaviors of agents/investors. Moreover, the recent information which investors have received is more informative compared to the historical information of long ago, and also the overall recent historical information, instead of only current instaneous information, affects the responses of agents/investors in the market.

In Chapter 5, we shall present a heterogeneous interacting agent model to study the emergence of empirical universal scaling properties observed in the real market [65]. In the model, all agents are coupled by the global variable – the price p_t of the single asset traded in the market. At each time step, all investors react (i.e., buy/sell/no trade) to the recent market price, and then the asset price in the market is updated according to the net demand on the asset. Each agent/investor goes through a two-step stochastic process to make his decision at each time step: first, he decides whether to trade on the asset or not, based on the deviation of current instantaneous asset price from its long-term average price, which behaves like S&P 500 or Nasdaq Composite to mimic the underlying true price interpreted by the market; second, the agent/investor decides to either buy or sell the asset if he has decided to trade on the asset. Therefore, all agents/investors behave like the spins in the Ising model, but all of them interact not directly but indirectly as compared in the Ising model [73, 74]. It is worth to note that the sensitivity to the asset price varies for different investors, this is why we call the model *heterogeneous* interacting agent model. In fact, such kind of heterogeneity just resembles the environmental variability applied in rock–paper–scissors models with spatial variability in previous chapters. In chapter 5, through Monte Carlo simulation on this heterogeneous interacting agents model [65], we recover the significant empirical phenomena such as volatility clustering, fat tail distribution of return and trading volume, and long-range correlation in volatility; meanwhile, we demonstrate that the emergence of fat-tail distribution of return is due to the long-tail distribution of trading volume resulted from the heterogeneity of investors [65].

Chapter 2

Spatial rock-paper-scissors models with inhomogeneous reaction rates

This chapter has been published in our paper [3]. We study several variants of the stochastic four-state rock–paper–scissors game or, equivalently, cyclic three-species predator–prey models with conserved total particle density, by means of Monte Carlo simulations on one- and two-dimensional lattices. Specifically, we investigate the influence of spatial variability of the reaction rates and site occupancy restrictions on the transient oscillations of the species densities and on spatial correlation functions in the quasi-stationary coexistence state. For small systems, we also numerically determine the dependence of typical extinction times on the number of lattice sites. In stark contrast with two-species stochastic Lotka–Volterra systems, we find that for our three-species models with cyclic competition quenched disorder in the reaction rates has very little effect on the dynamics and the long-time properties of the coexistence state. Similarly, we observe that site restriction only has a minor influence on the system's dynamical properties. Our results therefore demonstrate that the features of the spatial rock–paper–scissors system are remarkably robust with respect to model variations, and stochastic fluctuations as well as spatial correlations play a comparatively minor role.

2.1 Model and rate equations

The rock–paper–scissors (RPS) model describes the cyclic competition of three interacting species that we label A, B, and C. We consider the following (zero-sum [13]) predator–prey type interactions:

$$\begin{aligned} A+B &\to A+A \quad \text{with rate } k_a \ , \\ B+C &\to B+B \quad \text{with rate } k_b \ , \\ C+A &\to C+C \quad \text{with rate } k_c \ . \end{aligned} \tag{2.1}$$

Note that these irreversible reactions strictly conserve the total number of particles. We remark that naturally other variants of the RPS dynamics could also be considered; notably the four-state May–Leonard model which does not conserve the total particle density [75] has attracted considerable attention, see e.g. Refs. [13, 38, 76]. As will be demonstrated in Chapter 3, the conclusions presented here on the effects of carrying capacity and spatial reaction rate variability remain essentially unchanged for this system [2]. To generalize the above reaction model to a spatially extended lattice version, we allow empty sites (as a fourth possible state) and let the reactions happen only between nearest neighbors. In addition, we introduce nearest-neighbor particle hopping with rate D (if at most one particle is allowed per lattice site, this process takes place only if an adjacent empty site becomes selected at each time step).

Within the mean-field approximation, wherein any correlations and spatial variations are neglected, the following set of three coupled rate equations for homogeneous population densities $a(t)$, $b(t)$, and $c(t)$, with fixed total population density $a(t)+b(t)+c(t) = \rho = \text{const}$ describes the system's temporal evolution,

$$\begin{aligned} \partial_t\, a(t) &= a(t)\,[k_a\, b(t) - k_c\, c(t)]\ , \\ \partial_t\, b(t) &= b(t)\,[k_b\, c(t) - k_a\, a(t)]\ , \\ \partial_t\, c(t) &= c(t)\,[k_c\, a(t) - k_b\, b(t)]\ . \end{aligned} \tag{2.2}$$

These coupled rate equations possess a reactive fixed point, where all three species coexist, $(a^*, b^*, c^*) = (k_b, k_c, k_a)\rho/(k_a+k_b+k_c)$, which is marginally stable (see also Ref. [26]). Indeed, introducing new variables $\delta a(t) = a(t) - a^*$, $\delta b(t) = b(t) - b^*$, $\delta c(t) = c(t) - c^*$, and utilizing the conservation law $\delta a + \delta b + \delta c = 0$, we may express the first two rate equations in terms of δa and δb. Linearizing about the reactive fixed point then gives

$$\left(\begin{array}{c} \partial_t\, \delta a \\ \partial_t\, \delta b \end{array} \right) = L \left(\begin{array}{c} \delta a \\ \delta b \end{array} \right)\ , \tag{2.3}$$

with the linear stability matrix

$$L = \frac{\rho}{k_a + k_b + k_c} \left(\begin{array}{cc} k_b\, k_c & k_b\,(k_a + k_c) \\ -k_c\,(k_a + k_b) & -k_b\, k_c \end{array} \right)\ , \tag{2.4}$$

with eigenvalues $\lambda = \pm i\,\rho\,\sqrt{k_a\, k_b\, k_c/(k_a + k_b + k_c)} = \pm i\omega$, where $f = \omega/2\pi$ represents a characteristic oscillation frequency, e.g., for total density $\rho = 1$ and $k_a = 0.2$, $k_b = 0.5$, $k_c = 0.8$, $\lambda = \pm i\,2\sqrt{3}/15$, and the typical frequency is $f \approx 0.037$. We will use these mean-field values later to compare with the simulation results. In the special case of symmetric reaction rates where $k_a = k_b = k_c = k$, we get $\lambda = \pm i\,k/\sqrt{3}$; for example, if $\rho = 1$ and $k = 0.5$, then $\lambda = \pm i\,\sqrt{3}/6$ and $f \approx 0.046$. In addition, the system also has three absorbing states, with only a single species surviving ultimately: $(\rho, 0, 0)$, $(0, \rho, 0)$, and $(0, 0, \rho)$. Within the mean-field approximation, these fixed points are all linearly unstable. However, in any stochastic model realization on a finite lattice, temporal evolution would ultimately terminate in one of these absorbing states, as we shall explore for small systems below.

Model	Reaction rates	Site restriction
1	homogeneous rate: $k = 0.5$	no restriction
2	homogeneous rate: $k = 0.5$	at most one particle
3	uniform rate distribution	no restriction
4	uniform rate distribution	at most one particle

Table 2.1: List of stochastic lattice RPS model variants.

2.2 Monte Carlo simulation results

2.2.1 Model variants and quantities of interest

We investigate stochastic RPS systems on one- and two-dimensional lattices with periodic boundary conditions. At each time step, one individual of any species is selected at random, then hops to a nearest-neighbor site, if the chosen target site is empty. Otherwise, one of the particles on the chosen neighboring site is selected randomly and undergoes a reaction with the center particle according to the scheme and rates specified by (2.1) if both particles are different. The outcome of the reaction then replaces the eliminated particle. Note that predation reactions always involve neighboring particles; on-site reactions do not occur. This has the advantage of permitting us to treat the model variants with and without site occupation number restriction within the same setup, allowing for direct comparison. A similar approach was already adopted for the two-species lattice Lotka–Volterra model, where we have confirmed that nearest-neighbor predation interactions and strictly on-site reactions lead (without loss of generality) to essentially identical macroscopic features [46, 47].

If the selected and focal particle are of the same species, the center particle just hops to its chosen neighboring site. For our model variants with site occupancy restriction, the hopping process only takes place if the total number of particles on the target site is less than the maximum occupancy number (local carrying capacity) n_m. In this work, we set $n_m = 1$; i.e., each lattice site can either be empty or occupied by a single particle of either species A, B, or C (which gives four possible states for each site). Once on average each individual particle in the lattice has had the chance to react or move, one Monte Carlo step (MCS) is completed; thus the corresponding simulation time is increased by $\delta t \sim N^{-1}$. Also note that the hopping processes set the fundamental time scale; basically the reaction rates are measured in units of the diffusivity D (unless $D = 0$).

First, we shall study models with uniform symmetric reaction rates ($k_a = k_b = k_c = k = 0.5$); next we simulate systems with quenched spatial disorder by drawing the reaction probabilities k at each lattice site from a uniform distribution on the interval $[0, 1]$. Therefore, this distribution has the same mean reaction rate $1/2$ as the homogeneous rate in the model with fixed reaction rates, allowing for direct comparison of the relevant numerical quantities. The

four basic different model variants we have investigated are summarized in Table 2.1. In addition, we have studied systems with asymmetric reaction rates, both uniform and subject to quenched randomness with flat distribution. Besides the time-dependent population densities $a(t)$, $b(t)$, and $c(t)$, averaged over typically 50 individual simulation runs, we also investigate their corresponding temporal Fourier transforms

$$a(f) = \int a(t)\, e^{2\pi i f t}\, dt, \tag{2.5}$$

and the equal-time two-point occupation number correlation functions (cumulants)

$$C_{AB}(x,t) = \langle n_A(i+x,t)\, n_B(i,t)\rangle - a(t)\, b(t), \tag{2.6}$$

where i denotes the site index, and similarly for the other species, as well as $C_{AA}(x,t)$, etc. In addition, for small systems with N lattice sites we have numerically computed the mean extinction time $T_{\rm ex}(N)$ defined as the average time for the first of the three species to die out [77]. For the one-dimensional four-state RPS model, we have also determined the time evolution of the typical single-species domain size $\langle\lambda(t)\rangle$, see Sec. 2.2.4.

2.2.2 Two-dimensional stochastic RPS lattice models: symmetric rates

We first report and discuss our Monte Carlo simulation results on a 256×256 square lattice with periodic boundary conditions. The data are typically averaged over 50 Monte Carlo runs with different initial configurations, where the particles of each species are placed randomly on the lattice. Figure 2.1a depicts the temporal evolution of the total population densities in a system without site occupation number restrictions and with equal reaction rates $k_a = k_b = k_c = 0.5$ (labeled model 1 in Table 2.1), but unequal initial densities $a(0) = 2/3$, $b(0) = c(0) = 1/6$, along with two snapshots 2.1b,2.1c of their spatial distribution at different times. Since the selection and reproduction processes are combined into a single step in our model, the total population density ρ is strictly conserved, and as expected we therefore observe no spiral patterns that are characteristic of RPS models without conservation law [42]. In the initial time regime, we see distinct decaying population oscillations in Fig. 2.1a, and inhomogeneous species clusters in the snapshot Fig. 2.1b. As time progresses, the amplitude of the oscillating fluctuations decreases quickly, and also the spatial distribution and species cluster size become more stable and homogeneous (Fig. 2.1c). Our (fairly large) system eventually settles in a coexistence state with small density fluctuations (Fig. 2.1a inset). For comparison, Fig. 2.1d shows a snapshot in a system with identical reaction rates and asymmetric initial densities, but with all site occupation numbers restricted to at most a single particle (model 2); one observes the same small cluster structure as in the absence of occupation restrictions.

In Fig. 2.2 we show the absolute values of the Fourier transformed population density signals $|a(f)|$, as obtained from averaging 50 Monte Carlo simulation runs for the four different model

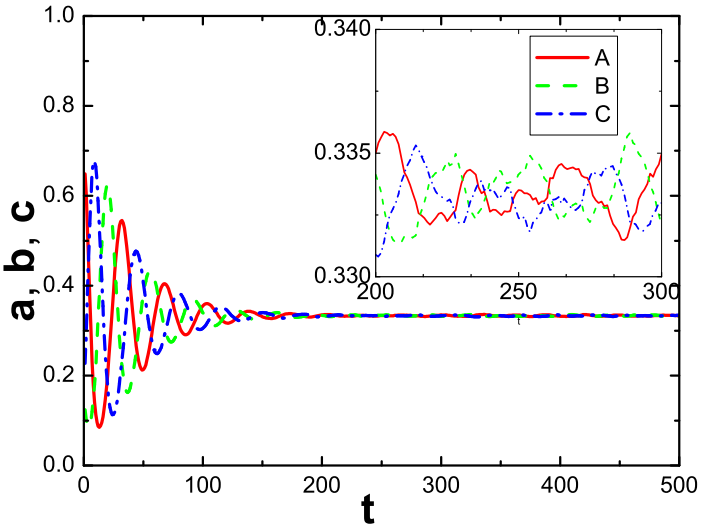

(a)

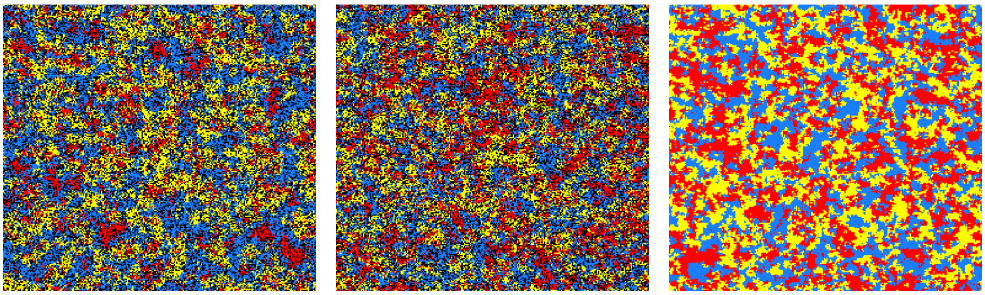

(b) (c) (d)

Figure 2.1: (a) Temporal evolution for the population densities of species A (red/solid line), B(green/dashed), and C (blue/dash-dotted) with symmetric reaction rates $k_a = k_b = k_c = 0.5$ and without site occupation restriction (model 1), with unequal initial densities $a(0) = 2/3$, $b(0) = c(0) = 1/6$, averaged over 50 Monte Carlo runs on a 256×256 square lattice. (b) Snapshot of the spatial particle distribution for a single simulation run at $t = 50$, and (c) at $t = 500$ MCS; (d): snapshot at $t = 500$ MCS, for a system where at most one particle of either species is allowed per site (model 2). (Color coding shows the majority species on each site; red/gray: species A, yellow/light gray: B, blue/dark gray: C, black: empty site.)

variants listed in Table 2.1, in this case with equal initial densities $a(0) = b(0) = c(0) = 1/3$. Recall that mean-field theory predicts a regular, undamped oscillation frequency $f \approx 0.046$. From the simulation data, we determine the characteristic peak frequency $f \approx 0.028$, which evidently governs oscillatory fluctuations; however, the finite width of the Fourier peak in

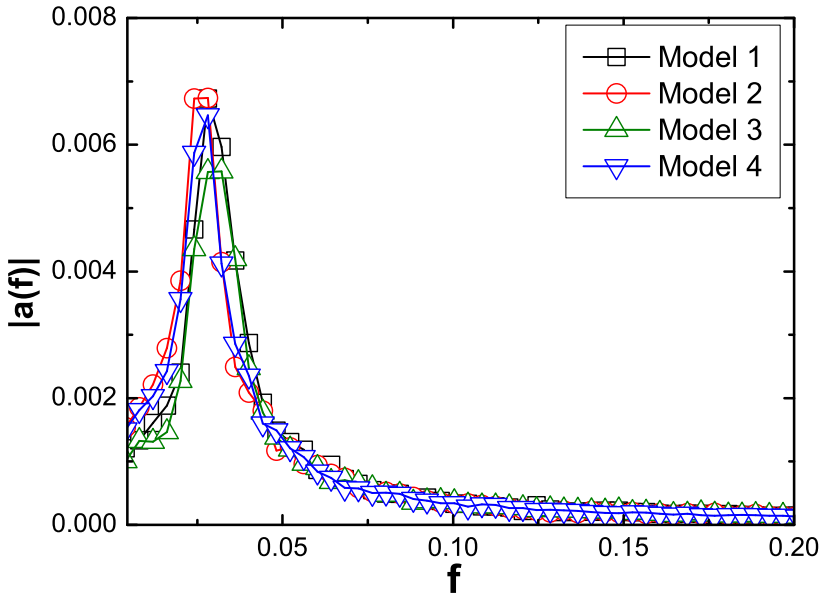

Figure 2.2: Signal Fourier transform $|a(f)|$ of species A density data on a 256×256 square lattice with initial population densities $a(0) = b(0) = c(0) = 1/3$ for the four model variants described in Table 2.1, averaged over 50 Monte Carlo simulation runs.

Fig. 2.2 reflects that the population oscillations are damped and will cease after a finite characteristic relaxation time.

Moreover, we see that even if spatial disorder and/or site occupancy restrictions are incorporated in the model, the Fourier-transformed density signals display practically the same frequency distribution and significant peak locations. Indeed, we find that in our simulations for model versions 1 and 3 with total density 1, the typical occupation number at each site remains $n \leq 2$ throughout the runs, which explains why the exclusion constraints in model variants 2 and 4 do not have a large effect. Thus, neither spatial disorder nor site occupancy restrictions change the temporal evolution pattern of the system markedly. This is in stark contrast with results for the two-species stochastic lattice Lotka–Volterra model, for which one finds (i) very pronounced spatio-temporal structures in the species coexistence regime [46]; (ii) large fluctuations that strongly renormalize the characteristic population oscillation frequency [46, 47]; (iii) an extinction threshold for the predator species induced by local density restrictions on the prey [46]; and (iv) considerable enhancement of the asymptotic densities of both species caused by spatial variability of the predation rate [48].

In order to study the effect of spatial disorder and site occupation restriction on emerging correlations in our stochastic RPS models, we have determined the equal-time two-point

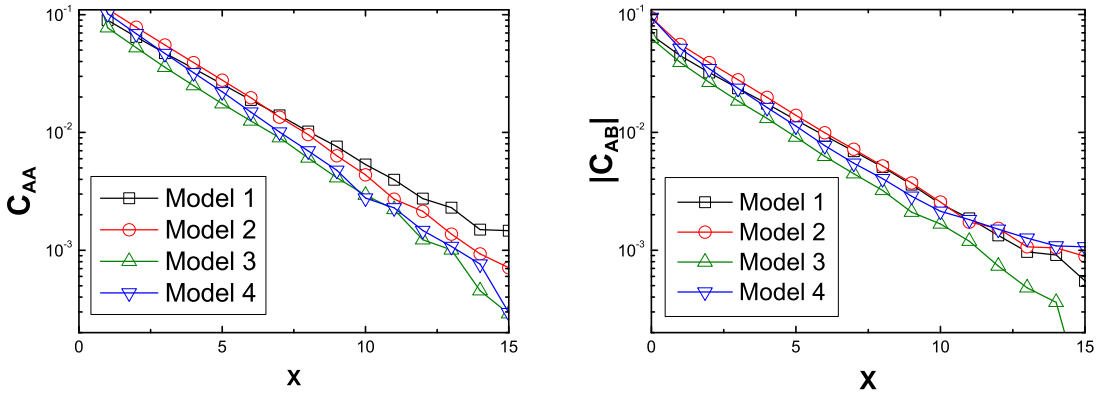

(a) (b)

Figure 2.3: (a) Static density autocorrelation function $C_{AA}(x)$ and (b) cross-correlation function $C_{AB}(x)$ (linear-log_{10} plots) measured at $t = 250$ MCS for the four model variants described in Table 2.1, with initial population densities $a(0) = b(0) = c(0) = 1/3$.

	Model 1	Model 2	Model 3	Model 4
l_{AA}	3.27 ± 0.02	2.92 ± 0.02	2.64 ± 0.03	2.59 ± 0.01
l_{AB}	2.86 ± 0.08	2.35 ± 0.09	2.40 ± 0.06	1.99 ± 0.09

Table 2.2: Correlation lengths l_{AA} for the autocorrelation function and l_{AB} for the cross-correlation function (in units of the lattice spacing) obtained for the four model variants of Table 2.1 with symmetric reaction rates.

correlation functions in the quasi-stationary (long-lived) coexistence state illustrated for models 1 and 2 in Figs. 2.1c and 2.1d, respectively. These static correlation functions can quantitatively capture the emerging spatial structures in the lattice. Figures 2.3a and 2.3b depict the autocorrelation function $C_{AA}(x)$ and the cross-correlation function $C_{AB}(x)$ as obtained for our four models (see Table 2.1), which all are seen to decay exponentially with distance, i.e., $C_{AA}(x) \propto e^{-|x|/l_{AA}}$ and $C_{AB}(x) \propto e^{-|x|/l_{AB}}$. From these log-normal plots, we have extracted the associated correlation length l_{AA} and typical species separation distance l_{AB}; the results are listed in Table 2.2. It is worth noticing that in systems exhibiting spiraling patterns, as in the four-state RPS model without conservation law, the correlation functions $C_{AA}(x)$ and $C_{AB}(x)$ do not fall off exponentially but exhibit (damped) oscillations, see e.g. Refs. [38, 40]. Site occupation restrictions clearly have the effect of reducing both correlation lengths. Also, as is the case for the two-species lattice Lotka–Volterra system [48], rendering the reaction rate a quenched random variable for each site leads to more localized population and activity patches, characterized by markedly smaller correlation and typical separation lengths.

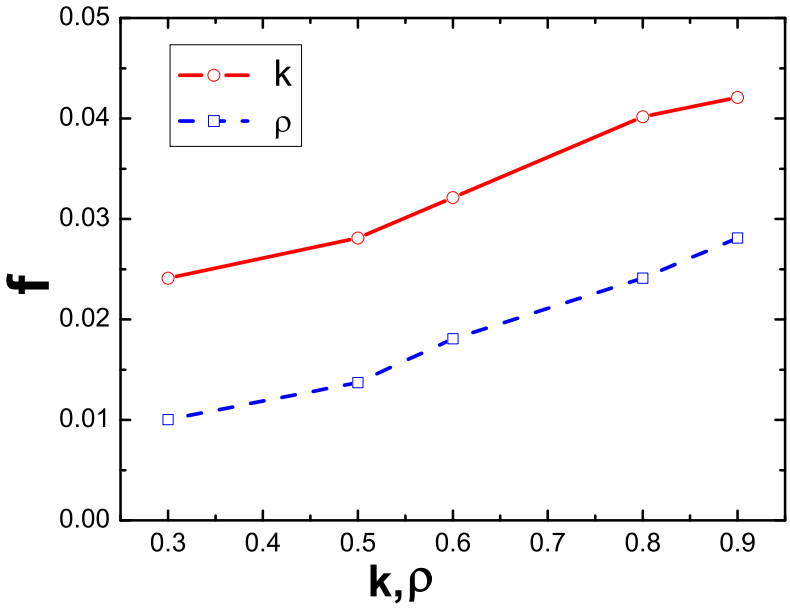

Figure 2.4: Variation of the characteristic peak frequency in the density Fourier signal $|a(f)|$ with the total density ρ and homogeneous, symmetric reaction rate k, for RPS simulations on a 256×256 square lattice with equal initial densities, run for 1000 MCS.

The influence of varying (homogeneous and symmetric) reaction rates and modifying the total (conserved) population density is explored in Fig. 2.4, which shows the dependence of the characteristic Fourier peak frequency f on k and ρ. We find that f scales roughly linearly with both the total density ρ and the reaction rate k, in accord with the mean-field prediction $f \propto \rho\, k$, see Sec. 2.1. We have also checked that switching off nearest-neighbor hopping (setting $D = 0$), thus allowing particle spreading only via the nonlinear reaction processes (2.1), essentially leaves the stochastic RPS system's features intact.

Finally, we have also studied the mean extinction time as function of lattice size N for small two-dimensional stochastic lattice RPS systems, here of the model 1 variety with homogeneous symmetric reaction rates $k_a = k_b = k_c = 0.5$ and equal initial densities $a(0) = b(0) = c(0) = 1/3$. We recall that in any finite system displaying an absorbing stationary state, stochastic fluctuations will eventually reach this absorbing configuration. In the stochastic RPS model, one therefore expects two species to eventually become extinct; however, reaching this absorbing state may take an enormous amount of time, and will thus become practically unobservable on large lattices. In fact, in two and higher dimensions one expects the mean extinction time $T_{\rm ex}$ (here measured for the first species to die out) to scale exponentially with system size N, since random fluctuations effectively have to over-

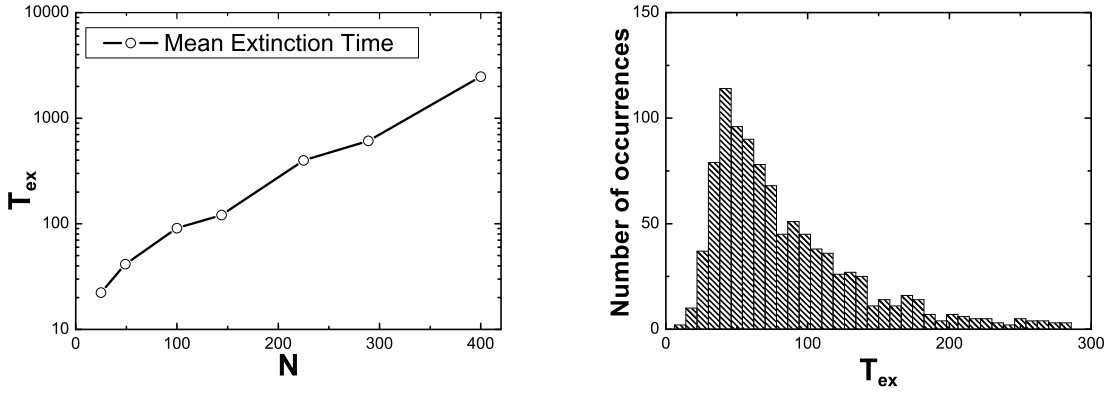

(a) (b)

Figure 2.5: (a) Mean extinction time as function of lattice size N (linear-log_{10} plot), obtained from averages over 50 Monte Carlo runs, for small two-dimensional lattice RPS systems in the absence of site restrictions and with symmetric reaction rates $k_a = k_b = k_c = 0.5$ (model 1), and equal initial population densities $a(0) = b(0) = c(0) = 1/3$. The data are for lattices with $N = 5 \times 5$, 7×7, 10×10, 12×12, 15×15, 17×17, and 20×20 sites. (b) Histogram of measured extinction times for $N = 100$ sites.

come a finite barrier in order to follow an 'optimal' path towards extinction. As depicted in Fig. 2.5a, we indeed observe $\ln T_{\rm ex}(N) \sim N$, consistent with the prediction on the coexistence state stability reported in Refs. [37, 40]. The associated distributions of extinction times are described by neither Poisson nor Gaussian distributions (e.g., the means are considerably larger than the most likely values), but display long 'fat' tails at large extinction times, see Fig. 2.5b. We expect similar features in model variant 2, in accord with the remarkably long-live species coexistence observed in Ref. [28].

2.2.3 Two-dimensional stochastic RPS system: asymmetric rates

Next we turn to a stochastic RPS system with asymmetric reaction rates and consider the various model variants specified in Table 2.3 together with the reactions (2.1). Figure 2.6a shows the time evolution for the three species' densities in a system with constant rates $k_a = 0.2$, $k_b = 0.5$, and $k_c = 0.8$. From our simulations for model version 1, we infer the asymptotic population densities (with statistical errors) $(0.40 \pm 0.01, 0.45 \pm 0.01, 0.15 \pm 0.01)$, which follow the trends of the mean-field results $(a^*, b^*, c^*) = (0.33, 0.53, 0.13)$. As becomes apparent in the snapshots 2.6b and 2.6c for model variant 1 without site restrictions, and 2.6d for a system with at most a single particle per site (model 2), particles of the same species form distinctive spatial clusters. The effect of the reaction rate asymmetry on the equal-time auto- and cross-correlation functions is shown in Figs. 2.7a and 2.7b, respectively, with the

Model	**Reaction rates**	**Site restriction**
1	$k_a = 0.2, k_b = 0.5, k_c = 0.8$	no restriction
2	$k_a = 0.2, k_b = 0.5, k_c = 0.8$	at most one
3	$k_a \in [0, 0.4]$, $k_b = 0.5$, $k_c = 0.8$	no restriction
4	$k_a \in [0, 0.4]$, $k_b = 0.5$, $k_c = 0.8$	at most one

Table 2.3: List of stochastic lattice RPS model variants with asymmetric rates. While $k_b = 0.5$ and $k_c = 0.8$ are held fixed in all four variants, we set $k_a = 0.2$ in models 1 and 2, whereas we took k_a to be a random variable uniformly distributed in $[0, 0.4]$ in models 3 and 4.

l_{AA}	l_{BB}	l_{CC}	l_{AB}	l_{BC}	l_{AC}
5.24 ± 0.03	5.67 ± 0.08	3.46±0.05	6.68 ± 0.20	3.68 ± 0.07	3.33 ± 0.05

Table 2.4: Correlation lengths inferred from the autocorrelation functions and typical separation distances obtained from the cross-correlation functions (in units of the lattice spacing) measured for the RPS model with asymmetric but homogeneous reaction rates $k_a = 0.2$, $k_b = 0.5$, and $k_c = 0.8$.

ensuing correlation lengths and typical separation distances listed in Table 2.4. Note that the autocorrelation length l_{CC} for species C is smaller than l_{AA}, and l_{BB}, which is largest. This is consistent with the long-time densities in the (quasi-stationary) coexistence state, given our observation that the overall particle density is roughly uniform.

As a last model variation, we allow the reaction rate k_a to be a quenched spatial random variable drawn from the flat distribution $[0, 0.4]$, such that its average is still 0.2, but hold $k_b = 0.5$ and $k_c = 0.8$ fixed. Fig. 2.8 compares the time evolution for these disordered systems with and without site restrictions with the corresponding homogeneous models. Once again, we see that spatial variability in the reaction rate even in this asymmetric setting has very little effect. As can be seen from the Fourier signal peak in Fig. 2.9, the characteristic frequency comes out to be $f \approx 0.021$ for all four asymmetric model variants investigated here, and Figs. 2.10a and 2.10b demonstrate that the disorder hardly modifies the spatial decay of the auto- and cross-correlation functions either.

2.2.4 One-dimensional Monte Carlo simulations

We have run simulations for all four model variants listed in Table 2.1, i.e., with/without site occupancy restriction; with/without quenched spatial randomness in the reaction rates, in one dimension. We find that only a single species ultimately survives and eventually occupies the whole lattice no matter whether spatial disorder or site restrictions are included

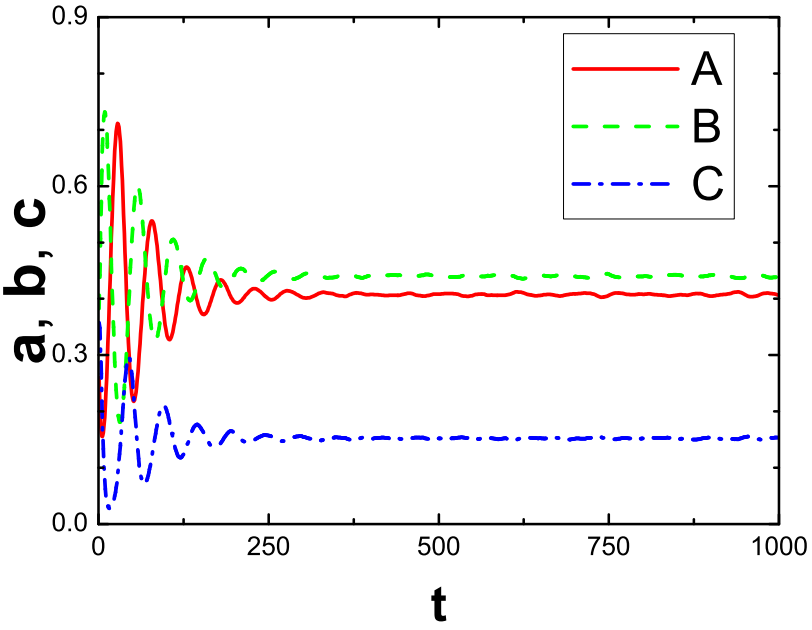

(a)

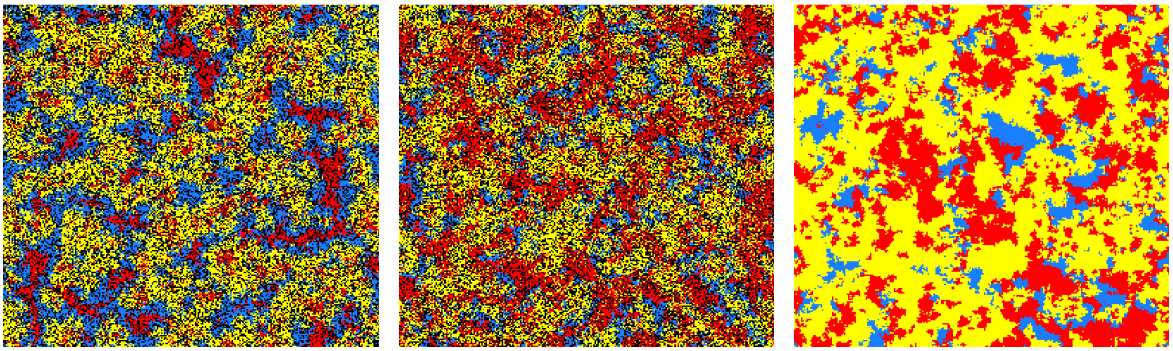

(b) (c) (d)

Figure 2.6: (a) Temporal evolution for the population densities of species A (red/solid line), B (green/dashed), and C (blue/dash-dotted) with asymmetric reaction rates $k_a = 0.2$, $k_b = 0.5$, $k_c = 0.8$ and without site occupation restriction (model 1), with equal initial densities $a(0) = b(0) = c(0) = 1/3$, averaged over 50 runs on a 256×256 square lattice. (b) Snapshot of the spatial particle distribution in a single simulation run at $t = 50$, and (c) at $t = 500$ MCS; (d): snapshot at $t = 500$ MCS, for a system where at most one particle of either species is allowed per site (model 2). (Majority species coloring: red/gray: A, yellow/light gray: B, blue/dark gray: C, black: empty.)

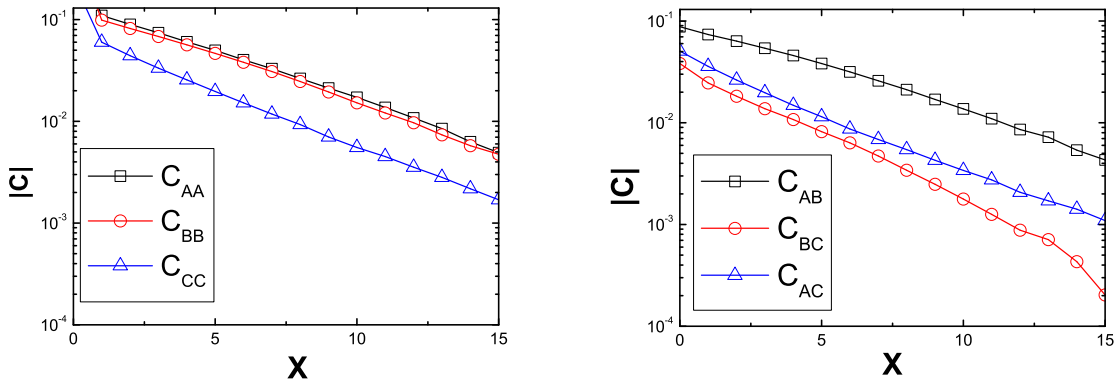

(a) (b)

Figure 2.7: (a) Equal-time autocorrelation functions $C_{AA}(x)$, $C_{BB}(x)$, $C_{CC}(x)$ at $t = 1000$ MCS for the model described in Fig. 2.6a. (b) Equal-time cross-correlation functions $C_{AB}(x)$, $C_{BC}(x)$, $C_{AC}(x)$ (linear-log_{10} plots).

in the model: as expected, the one-dimensional system will always evolve towards one of the three extinction states where two of the three species will die out (However, it is worth mentioning that strongly enhanced particle pair exchange processes can lead to a mean-field like coexistence even in one-dimensional systems [32]). While this phenomenon also occurs in two dimensions, in $d = 1$ the species coexist over a time that on average scales polynomially with the system size (see below), i.e., extinction happens on a much shorter time scale than in two dimensions (see Fig. 2.5a). Again, for equal (mean) reaction rates and initial densities, each species has equal survival probability. For comparison, the space-time plots of one-dimensional lattice simulations without and with site occupancy restriction are depicted in Figs. 2.11 and 2.12, respectively. It is seen that individuals of identical species cluster together, and any reactions are confined to the boundary separating the single-species domains. When the occupancy of any site is restricted to a single particle of either species, these domains form quickly and are very robust, even if not all sites are filled, see Figs. 2.12a and 2.12b.

The population density signal Fourier transform $|a(f)|$, shown for species A in Fig. 2.13, confirms the absence of any population oscillations through the absence of any peak at nonzero frequency f, and the width of the peak at $f = 0$ reflects the decay time to the stationary extinction state. As in two dimensions, we observe very little effect of either site occupation number restrictions or spatial variability of the reaction rates on the Fourier signal, compare Figs. 2.2 and 2.9. We have also measured the mean single-species domain size $\langle\lambda(t)\rangle$ and investigated its growth with time t, shown in Fig. 2.14. As was predicted in Refs. [29, 30], for the implementation with site occupancy restriction (model 2) to at most a single particle per site, we observe $\langle\lambda(t)\rangle \sim t^{3/4}$; we find the same asymptotic growth law

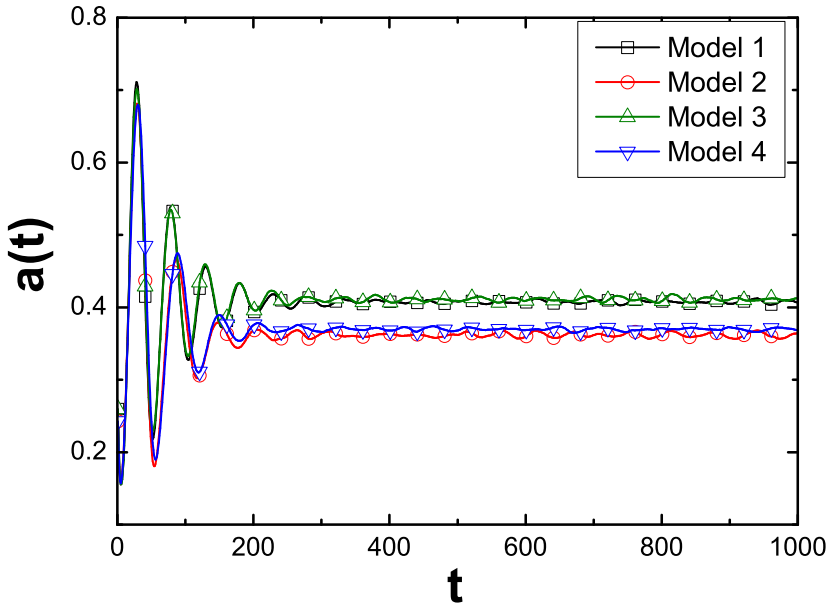

Figure 2.8: Time evolution for the population density $a(t)$ of species A for four model variants with asymmetric reaction rates, namely with $k_b = 0.5$, $k_c = 0.8$ and either uniformly $k_a = 0.2$, or drawn from a flat distribution $[0, 0.4]$, with and without site restrictions (see the listing in Table 2.3). The initial densities are $a(0) = b(0) = c(0) = 1/3$, and the data stem from averages over 50 runs on a 256×256 square lattice.

when arbitrarily many particles are allowed on each lattice site. An algebraic decay of the number of domains was also reported in Ref. [28]. The domain stability is further illustrated by the very slow temporal decay of the on-site auto- and cross-correlation functions (see Figs. 2.15a and 2.15b). Notice that quenched spatial disorder in the reaction rates does not affect the time evolution of the autocorrelation functions, in contrast with site occupancy restrictions; here the results depend on the presence or absence of empty sites, see Fig. 2.15a. However, the cross-correlation functions in Fig. 2.15b look essentially indistinguishable for all these model variations.

Figures 2.16a and 2.16b respectively depict the equal-time auto- and cross-correlation functions for the various model variants listed in Table 2.1 obtained for a one-dimensional lattice with 50000 sites. We observe exponential decay with similar large correlation lengths for all model variants upto about 50 lattice sites, followed by a cutoff (which extends to larger x as time increases).

Finally, we investigate the mean extinction time as function of system size N in one dimension. As becomes apparent in Figs. 2.17a, in all one-dimensional model variants we have

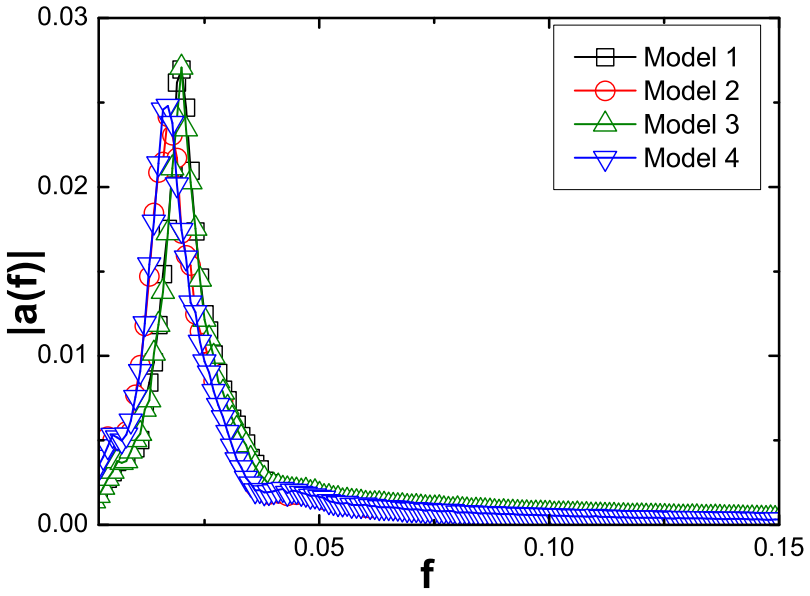

Figure 2.9: Signal Fourier transform $|a(f)|$ for the four model variants described in Table 2.3. The characteristic frequency comes out to be $f \approx 0.021$.

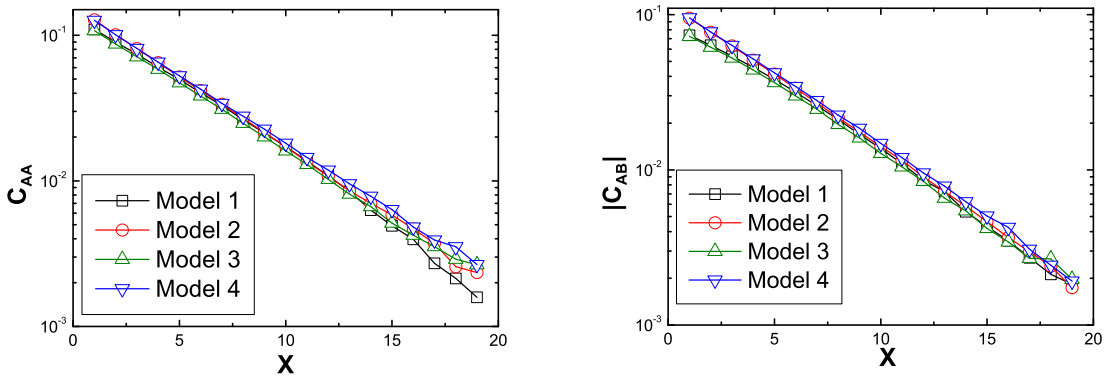

(a) (b)

Figure 2.10: (a) Equal-time autocorrelation function $C_{AA}(x)$ and (b) cross-correlation functions $C_{AB}(x)$ (linear-log_{10} plots) at $t = 1000$ MCS for the four model variants described in Table 2.3.

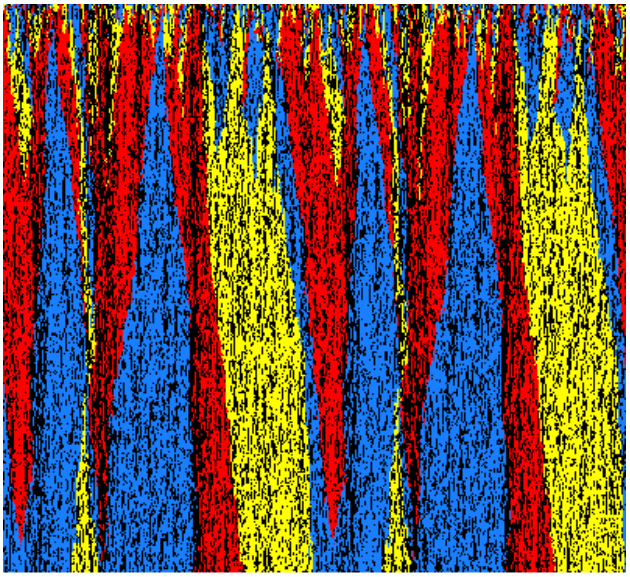

Figure 2.11: Time evolution (up to 1000 Monte Carlo steps; from top to bottom) for a one-dimensional RPS model run with equal, homogeneous reaction rates $k_a = k_b = k_c = 0.5$, equal initial densities $a(0) = b(0) = c(0) = 1/3$, and in the absence of site occupancy restriction. (Only 10000 of the total 50000 lattice sites in this run are shown; majority species coloring in red/gray: A, yellow/light gray: B, blue/dark gray: C, black: empty.)

considered, within our (large) error bars the mean extinction time appears to follow a power law $T_{\rm ex} \sim N^{\gamma}$, as proposed in Refs. [25, 45, 77, 78]. However, a best power-law fit yields variable effective exponents $T_{\rm ex} \sim N^{\gamma}$ with γ ranging from ~ 1.5 to ~ 1.8 if we fit the data up to $N = 50$ or $N = 200$, respectively, rather than $\gamma = 2$ [77] or $\gamma = 1$ [25, 45, 78]. Biasing the data towards smaller systems for which the statistical errors are likely better controlled, our results may even be consistent with the mean-field value $\gamma = 1$. Note, however, that the extinction time distribution acquires even fatter tails at large times than in two dimensions, see Fig. 2.17b, and rare long survival events dominate the averages and induce large statistical fluctuations. The mean extinction time alone therefore poorly characterizes the extinction kinetics. When the reaction rates are chosen asymmetric, we have checked that only the 'weakest' species with the smallest predation rate survives, whereas the other two species are driven to extinction [26, 27].

2.3 Summary

In this chapter, we have studied the effects of finite carrying capacity and spatial variability in the reaction rates on the dynamics of a class of spatial rock–paper–scissors (RPS) models. We have investigated the properties of several variants of the stochastic four-state zero-sum

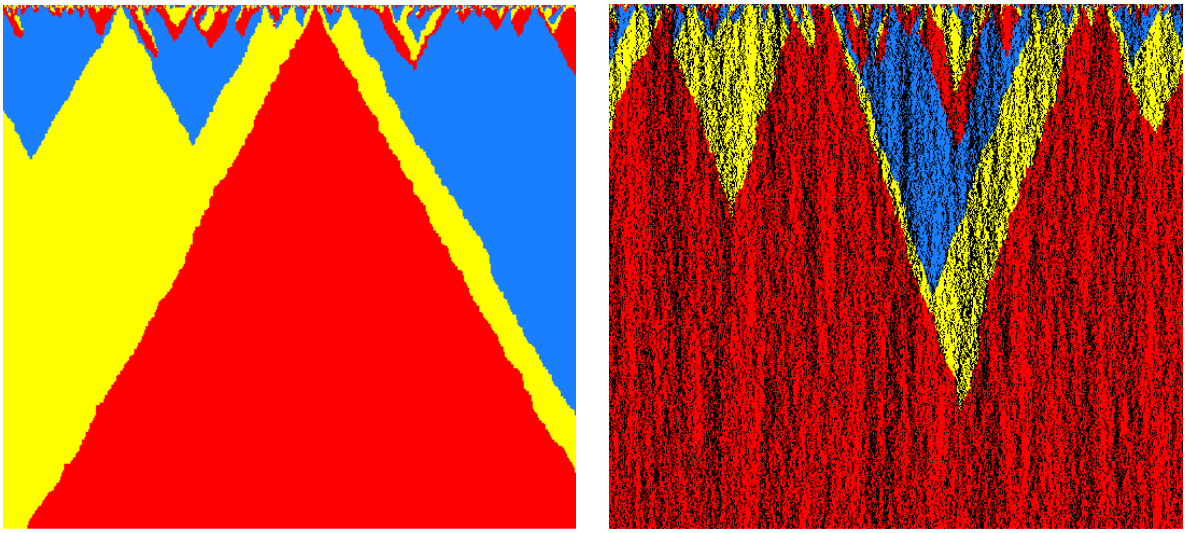

(a) (b)

Figure 2.12: Time evolution (up to 1000 Monte Carlo steps; from top to bottom) for one-dimensional RPS model runs with equal, homogeneous reaction rates $k_a = k_b = k_c = 0.5$, equal initial densities (a) model 2: $a(0) = b(0) = c(0) = 1/3$, and (b) model 2': $a(0) = b(0) = c(0) = 0.2$ (model 2' and 4' refer to the corresponding model variants listed in Table 2.1 with total particle density less than 1), where at most one particle of either species is allowed per site. (Only 10000 of the total 50000 lattice sites in these runs are shown; red/gray: A, yellow/light gray: B, blue/dark gray: C, black: empty.)

RPS game (with conserved total particle number) on two- and one-dimensional lattices with periodic boundary conditions. In two dimensions, owing to the strict (local) conservation of the total particle number, one does not observe the formation of spiral patterns; the three species simply form small clusters. In fact, spatial correlations are weak in the (quasi-stationary) coexistence state, and the system is remarkably well described by the mean-field rate equation approximation. Typical extinction times scale exponentially with system size [37, 38, 40], resulting in coexistence of all three species already on moderately large lattices. We find the characteristic initial oscillation frequency to be proportional to the reaction rate and total particle density, as predicted by mean-field theory.

We observe that neither site occupation number restrictions nor quenched spatial disorder in the reaction rates markedly modify the populations' temporal evolution, species density Fourier signals, or equal-time spatial correlation functions. This observation holds for models with symmetric as well as asymmetric reaction rates, and even if spatial variability is introduced only for the competition of one species pair. On the basis of the mean-field results, this very weak disorder effect is a consequence of the essentially *linear* dependence of the long-time densities on the reaction rates k; averaging over a symmetric distribution just yields the average. In the two-species Lotka–Volterra model, instead both the asymptotic

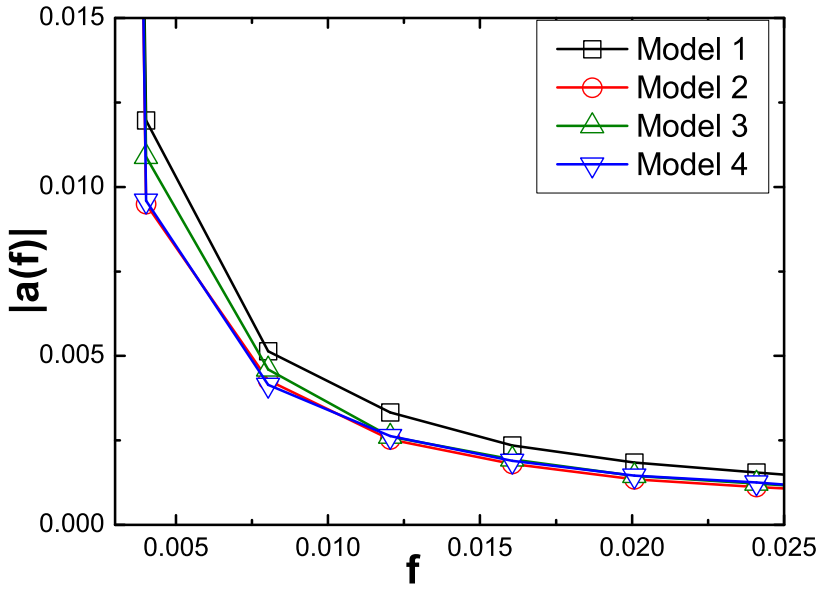

Figure 2.13: Signal Fourier transform $|a(f)|$ for the four RPS model variants listed in Table 2.1, in one dimension. The data is averaged over 50 Monte Carlo simulations on lattices with 50000 sites.

predator and prey densities are inversely proportional to the predation rate, and averaging over a distribution of the latter strongly biases towards small rate values and large densities [48]. Both in the two- and cyclic three-species systems, spatially variable rates induce stronger localization of the species clusters.

In one dimension, two species are driven towards extinction with the mean extinction time $T_{\text{ex}} \sim N^{\gamma}$, $\gamma \approx 1 \ldots 1.8$ (with large error bars), and only a single species survives. The distribution of extinction times displays fat long-time tails. We confirm that the single-species domains grow with the predicted power law $\langle \lambda(t) \rangle \sim t^{3/4}$ in the models with site restrictions [29, 30], and we have obtained similar results for the model variants with an infinite carrying capacity. For asymmetric reaction rates, we have also checked that the 'weakest' species is the surviving one [26, 27].

Our results demonstrate that the physical properties of cyclic RPS models are quite robust, even quantitatively, with respect to modifications of their 'microscopic' model definitions and characterization. This is in stark contrast with the related two-species Lotka–Volterra predator-prey interaction model. We believe the origin of this remarkable robustness lies in the comparatively weaker prominence of stochastic fluctuations and spatial correlations in the cyclic three-species system. The robustness of the RPS models considered here implies

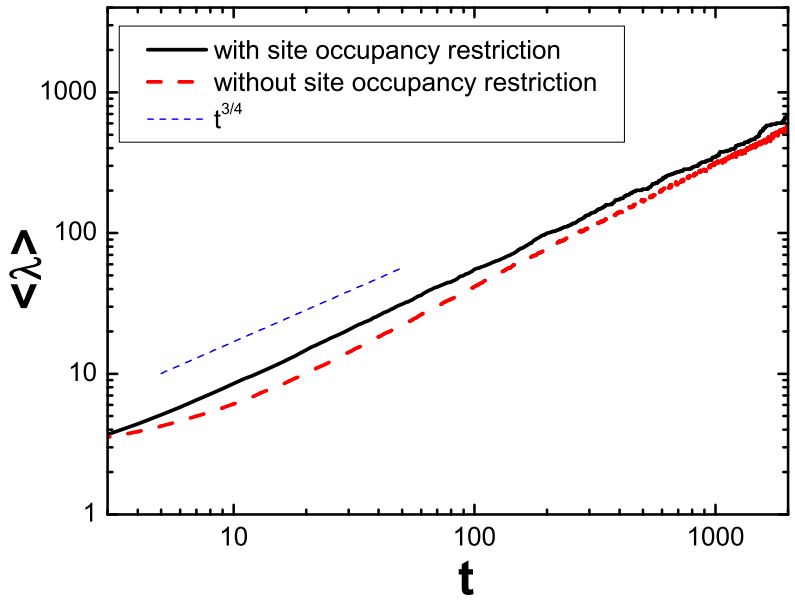

Figure 2.14: The time evolution ($log_{10} - log_{10}$ plot) of the mean single-species domain size $\langle\lambda(t)\rangle$ measured in one-dimensional Monte Carlo simulation runs with 10000 lattice sites for RPS models with symmetric reaction rates $k_a = k_b = k_c = 0.5$ and equal initial densities $a(0) = b(0) = c(0) = 1/3$. The upper (black) curve shows the data for model 2 with site occupation restriction, see Fig. 2.12a, whereas the lower (red/dashed) graph pertains to model variant 1 without site occupancy restrictions, see Fig. 2.11. For comparison, the blue/dotted straight line represents the predicted $t^{3/4}$ power law [29, 30].

that environmental noise can be safely ignored and that their properties are essentially independent of the carrying capacity. It is worth emphasizing that this result is nontrivial; in terms of modeling such systems, it notably implies that one has the freedom to consider strict site restriction ($n_m = 1$) and hence simplify the numerical calculations, or to set $n_m = \infty$ (no site restrictions) and thus facilitate the mathematical treatment. In fact, our study establishes that both 'microscopic' model realizations are essentially equivalent. As it turns out, this conclusion also pertains to spatial May–Leonard models [75, 76], as we shall report in Chapter 3.

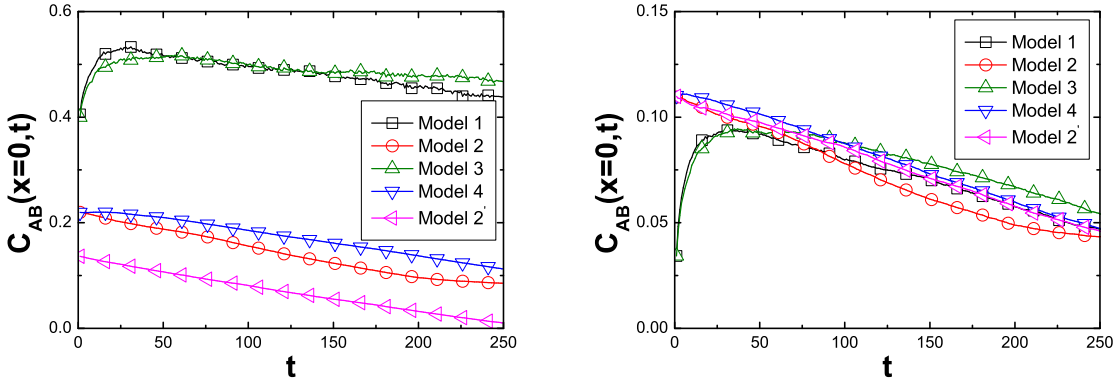

(a) (b)

Figure 2.15: Time evolution for the on-site (a) autocorrelation $C_{AA}(0,t)$ and (b) cross-correlation function $C_{AB}(0,t)$ in one-dimensional RPS model variants with 500 sites, averaged over 1000 simulation runs. Shown are the results for model variants 1–4 with initial densities $a(0) = b(0) = c(0) = 1/3$; model 2' refers to a system with site occupancy restriction 1 and lower particle density $a(0) = b(0) = c(0) = 1/4$.

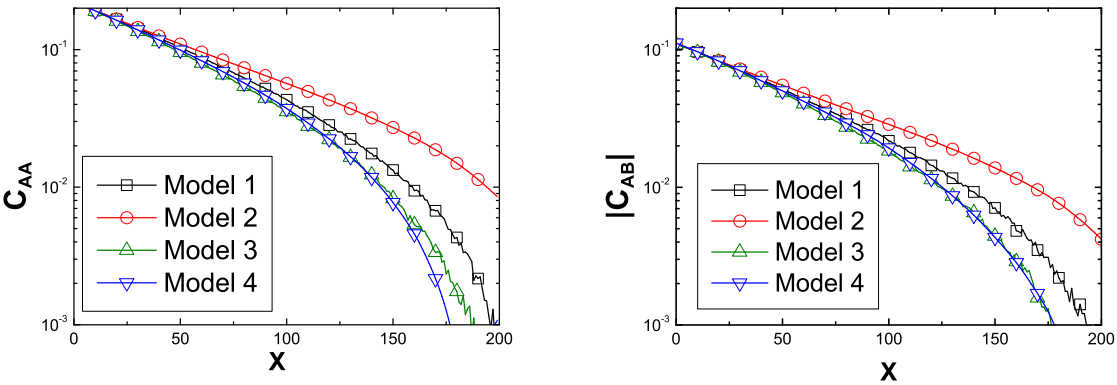

(a) (b)

Figure 2.16: (a) Static autocorrelation functions $C_{AA}(x)$ and (b) static cross-correlation functions $C_{AB}(x)$ (linear-log_{10} plots) measured at $t = 250$ MCS for the four RPS model variants described in Table 2.1 on a one-dimensional lattice with 50000 sites, averaged over 50 simulation runs.

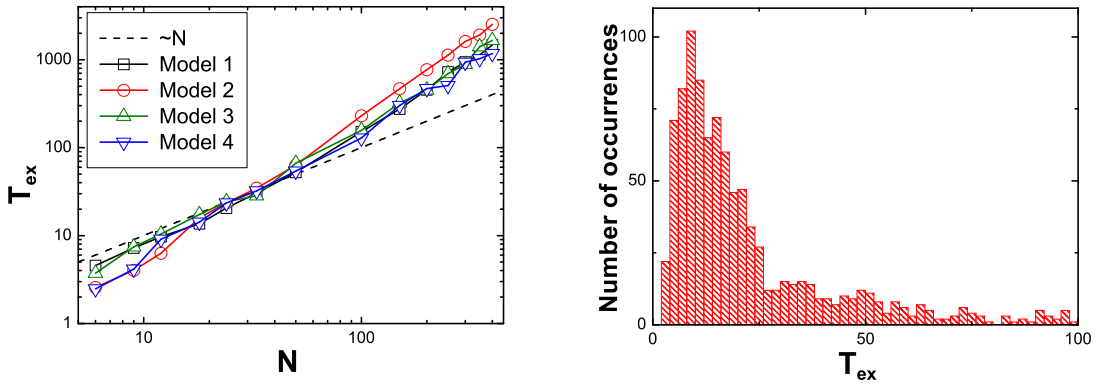

(a) (b)

Figure 2.17: (a) Mean extinction time as function of lattice size N ($log_{10} - log_{10}$ plot), obtained from averages over 1000 Monte Carlo runs, in one dimension. (b) Histogram of the measured extinction times for model variant 2 with $N = 30$; compare with Figs. 2.5a and 2.5b.

Chapter 3

Coexistence in the two-dimensional May–Leonard model with random rates

This chapter has been published in our paper [2]. In this chapter, we employ Monte Carlo simulations to numerically study the temporal evolution and transient oscillations of the population densities, the associated frequency power spectra, and the spatial correlation functions in the (quasi-)steady state in two-dimensional stochastic May–Leonard models of mobile individuals, allowing for particle exchanges with nearest-neighbors and hopping onto empty sites. We therefore consider a class of four-state three-species cyclic predator-prey models whose total particle number is not conserved. We demonstrate that quenched disorder in either the reaction or in the mobility rates hardly impacts the dynamical evolution, the emergence and structure of spiral patterns, or the mean extinction time in this system. We also show that direct particle pair exchange processes promote the formation of regular spiral structures. Moreover, upon increasing the rates of mobility, we observe a remarkable change in the extinction properties in the May–Leonard system (for small system sizes): (1) As the mobility rate exceeds a threshold that separates a species coexistence (quasi-) steady state from an absorbing state, the mean extinction time as function of system size N crosses over from a functional form $\sim e^{cN}/N$ (where c is a constant) to a linear dependence; (2) the measured histogram of extinction times displays a corresponding crossover from an (approximately) exponential to a Gaussian distribution. The latter results are found to hold true also when the mobility rates are randomly distributed.

3.1 Model and rate equations

In the mean-field approximation, our spatial system reduces to the original May–Leonard model[1] [75]. We let all populations live on a square lattice, with each lattice site occupied with at most a single individual. We therefore allow four states per site: three interacting particle species that we label A, B, and C, and an empty state $\emptyset$. The model is defined through the following set of binary predation and offspring production reactions between the three particle species [37, 38, 75]:

$$\begin{aligned} A + B &\to \emptyset + A \qquad \text{with rate } \sigma \ ; \\ B + C &\to \emptyset + B \qquad \text{with rate } \sigma \ ; \\ C + A &\to \emptyset + C \qquad \text{with rate } \sigma \ ; \end{aligned} \tag{3.1}$$

$$X + \emptyset \to X + X \qquad \text{with rate } \mu \ , \tag{3.2}$$

where $X \in (A, B, C)$ refers to any one of the three species. Note that in contrast with the conventional rock–paper–scissors model [3, 25, 39, 79, 80, 81], the total particle number is *not* conserved by these reactions, owing to the separation of predation and reproduction processes. In addition, in our spatially-extended system we consider the nearest-neighbor particle exchange and hopping processes on a two-dimensional square lattice (with periodic boundary conditions; here again $X, Y = A, B, C$):

$$X + Y \to Y + X \qquad \text{exchange rate } \epsilon \ ; \tag{3.3}$$

$$X + \emptyset \to \emptyset + X \qquad \text{hopping rate } D \ . \tag{3.4}$$

It is worth mentioning that the models studied in Refs. [37, 38, 40] do not separate the hopping process (3.4) from pair exchange (3.3); i.e., $\epsilon = D$. Therefore, when letting $\epsilon = D$ and in the absence of any quenched disorder, our spatial model coincides with the one investigated in Refs. [37, 38, 40].

May and Leonard [75] studied the associated deterministic mean-field rate equations and obtained the temporal evolution of the population densities. Let $a(t)$, $b(t)$, and $c(t)$ represent the population densities (concentrations) of species A, B, and C, respectively. Since at most one individual is allowed on each site in the simulation, within the mean-field approximation, the overall population density $\rho(t) = a(t) + b(t) + c(t)$ restricts the reproduction processes (3.2). Therefore, the corresponding rate equations are

$$\begin{aligned} \partial_t \, a(t) &= a(t) \left[\mu \left(1 - \rho(t) \right) - \sigma \, c(t) \right] \ , \\ \partial_t \, b(t) &= b(t) \left[\mu \left(1 - \rho(t) \right) - \sigma \, a(t) \right] \ , \\ \partial_t \, c(t) &= c(t) \left[\mu \left(1 - \rho(t) \right) - \sigma \, b(t) \right] \ . \end{aligned} \tag{3.5}$$

[1] At the mean-field level, the model considered here corresponds to the original May–Leonard model [75] with parameters $\alpha = 1$ and $\beta = 1 + \sigma/\mu$, and time measured in units of $1/\mu$.

The coupled rate equations (3.5) yield four linearly unstable absorbing states $(a, b, c) = (0, 0, 0)$, $(1, 0, 0)$, $(0, 1, 0)$, and $(0, 0, 1)$, and one reactive fixed point $(a^*, b^*, c^*) = \frac{\rho^*}{3}(1, 1, 1)$, where $\rho^* = \frac{3\mu}{3\mu+\sigma}$, representing coexistence between the three species. Linearizing around the coexistence fixed point leads to

$$\begin{pmatrix} \partial_t\, \delta a \\ \partial_t\, \delta b \\ \partial_t\, \delta c \end{pmatrix} = L \begin{pmatrix} \delta a \\ \delta b \\ \delta c \end{pmatrix} \ , \tag{3.6}$$

where $\delta a(t) = a(t) - a^*$, $\delta b(t) = b(t) - b^*$, and $\delta c(t) = c(t) - c^*$, and with the linear stability matrix L

$$L = \frac{-\mu}{3\mu+\sigma} \begin{pmatrix} \mu & \mu & \mu+\sigma \\ \mu+\sigma & \mu & \mu \\ \mu & \mu+\sigma & \mu \end{pmatrix} \ . \tag{3.7}$$

Its eigenvalues are $\lambda_1 = -\mu$, and $\lambda_{2,3} = \frac{\mu\sigma}{2(3\mu+\sigma)}[1 \pm \sqrt{3}i]$, which demonstrates that the fixed point is locally stable only in one direction of parameter space (the eigenvector associated with the negative eigenvalue λ_1), and generally linearly unstable. As elaborated in Refs. [37, 38, 40], the system dynamics quickly approaches an invariant manifold associated with the rate equations (3.5). In the neighborhood of the unstable interior fixed point (a^*, b^*, c^*), the invariant manifold is tangent to the plane normal to the eigenvector of L associated with λ_1 [40]. On this invariant manifold, the trajectories approach the absorbing boundaries of the phase portrait where they linger and form a heteroclinic cycle [13, 75]. In this case, any chance fluctuations can cause species extinction by deviating the trajectories toward the absorbing boundaries. From the imaginary part of the complex conjugate eigenvalues $\lambda_{2,3}$, we infer the characteristic oscillation frequency $\omega = \sigma\rho^*/(2\sqrt{3})$.

3.2 Monte Carlo simulation results for the spatially-extended May-Leonard model

We investigate the two-dimensional May–Leonard model, i.e., the four–state stochastic RPS game defined by the reactions (3.1,3.2) (which do not conserve the total particle number) on a two-dimensional lattice (typically with $N = 256 \times 256$ sites) with periodic boundary conditions, subject to the nearest-neighbor exchange (3.3) and hopping (3.4) processes. In order to mimic finite local carrying capacities, we impose a maximum occupancy number of one particle (of either species) per lattice site. When investigating the effect of spatial disorder on the model, we will treat one of the rates (μ, σ, ϵ, or D) at each lattice site as a random number drawn from a normalized Gaussian distribution truncated at one standard deviation on both sides (Similar simulation results are observed when employing uniform distribution instead of Gaussian distribution to study the influence of spatial disorder). For example, $\mu \sim N(m, n)$ implies that the rate μ is picked from a truncated normal distribution

on the interval $[m-n, m+n]$, centered at the value m with standard deviation $n < m$. In practice, a value of μ is drawn from $N(m, n)$ for each site on the lattice and attached to the corresponding site at the beginning of each single Monte Carlo run. The rate values remain unchanged for all sites until the next run is initiated. Therefore, in our model, the randomized rates pertain to the lattice sites; but are identical for any individual landing on a given site for each single run.

At each simulation step, an individual of any species on the lattice is selected randomly; then one of its four nearest-neighbor sites, which might be empty or occupied by one particle of either three species, is selected at random. Subsequently, the particles undergo the pair reaction (3.1), reproduction (3.2), exchange (3.3), or hopping (3.4) processes, according to the respective associated rates. Once on average each of the P individual particles on the lattice has had a chance to react, reproduce, exchange, or move, one Monte Carlo step (MCS) is completed; the infinitesimal simulation time step is thus $\delta t \sim P^{-1}$. Due to lack of conservation law in the system, P is not a constant so that the infinitesimal simulation time step δt does not remain unchanged in the simulation.

When studying the effect of quenched spatial disorder in the reaction and mobility rates, we shall focus on investigating a base model with (average) mobility rate set to 5, since the corresponding pure system displays clearly established spiral waves (see Fig. 3.1b below). Whenever neither fixed rate values nor their distribution are specified below, the following default rate values were implemented in the simulations: $\mu = \sigma = 1$, and $\epsilon = D = 5$. We shall characterize the emerging spatial structures through instantaneous snapshots of the particle distribution in the lattice, and will depict the temporal evolution of population (spatially averaged) densities. Because of the underlying symmetry among the species A, B, and C, one representative population suffices and we here report results for the spatial average of local population number $n_A(j,t)$ of species A, i.e., the spatially averaged density $a(t) = \langle n_A(j,t) \rangle = \frac{1}{N} \sum_j n_A(j,t)$, where j represents the site index. We shall also obtain the associated Fourier transform $a(f)$ (see the definition in (2.5)) and compute the equal-time two-point correlation functions in the (quasi-)steady state, e.g., $C_{AB}(x,t)$ and $C_{AA}(x,t)$ (see the definition in (2.6)). For our typical system size of $N = 256 \times 256$ sites we never observed the extinction state in our simulations. In fact, as discussed in Ref. [37] and below (see Sec. 3.3.3), in this case one expects the extinction time to grow exponentially with the system size. Therefore, in order to access absorbing states and numerically measure the mean extinction time (MET) $\bar{T}_{\rm ex} = \langle T_{\rm ex} \rangle$, where $T_{\rm ex}$ is the extinction time for a single Monte Carlo run, and extract extinction time distributions, we must consider small systems of sizes $N = 25$ to 225.

3.2.1 Self-organization in the three-species coexistence phase

In the first row of Fig. 3.1, we plot typical snapshots of the spatial particle distributions at $t = 1000$ MCS for various exchange and diffusion rates, as indicated, while $\mu = \sigma = 1$

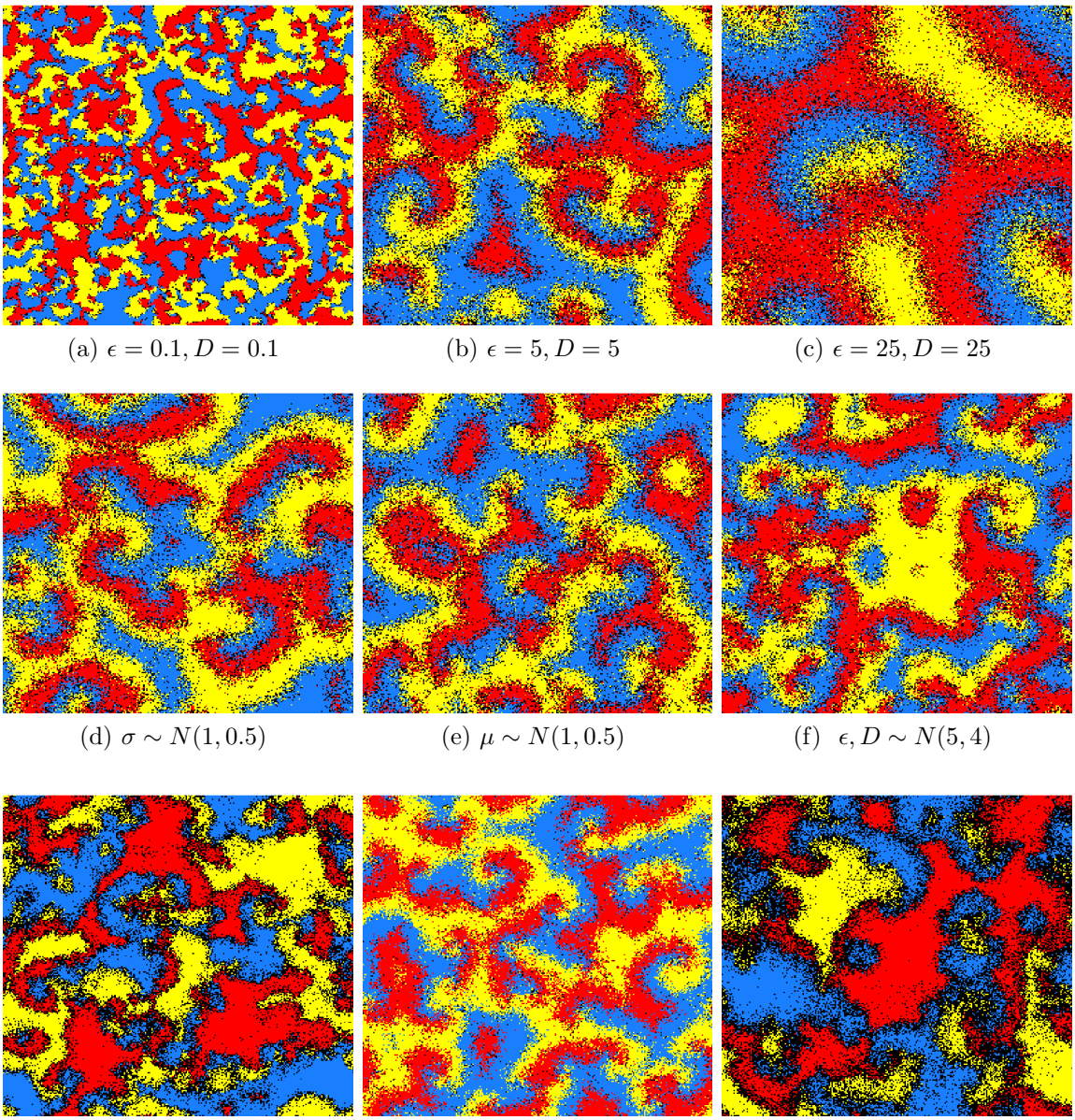

(a) $\epsilon = 0.1, D = 0.1$ (b) $\epsilon = 5, D = 5$ (c) $\epsilon = 25, D = 25$

(d) $\sigma \sim N(1, 0.5)$ (e) $\mu \sim N(1, 0.5)$ (f) $\epsilon, D \sim N(5, 4)$

(g) $\epsilon = 0, D = 5$ (h) $\epsilon = 5,\ D = 0$ (i) $\epsilon = 0,\ D = 25$

Figure 3.1: Snapshots of the spatial particle distribution at $t = 1000$ MCS for a system with $N = 256 \times 256$ sites with equal initial densities $a(0) = b(0) = c(0) = 1/3$. If not specified otherwise, the corresponding default rate values are implemented $\mu = \sigma = 1$, $\epsilon = D = 5$. (red/gray: A, yellow/light gray: B, blue/dark gray: C, black: empty).

are held fixed. We observe in Fig. 3.1a that all three species coexist and a set of entangled spiral patterns forms in the system when the mobility rates are comparatively low. Upon

increasing the mobility rates, the spiral patterns expand, see Fig. 3.1b. When the spirals' typical size ℓ at last outgrows the lattice for large particle mobility (compare Fig. 3.1a–3.1c), we anticipate that the system essentially acquires the features of its zero-dimensional stochastic counterpart (see Sec. 3.3.3 and Ref. [37]). In that situation, the system evolves towards one of the three absorbing states wherein two species become extinct, and the surviving species uniformly fills the lattice (uniform phase). In finite systems therefore, there exists a threshold set by the condition $\ell \approx L = \sqrt{N}$ (in a square lattice) that separates the absorbing states from species coexistence. Since the typical extent of the spirals grow diffusively as $\ell \sim \sqrt{2\epsilon}, \sqrt{2D}$, this transition should occur at some critical value M_c of the scaled effective mobility $M = 2(\epsilon, D)/N$ [37].

In two-species predator-prey systems, quenched spatial disorder in the reaction rates can markedly enhance both asymptotic particle densities in two-species predator-prey systems [48]; yet this finding is not corroborated in three-species RPS models with conserved total population [3]. Thus we next explore the effect of spatial variability in the reaction as well as in the mobility rates in the spatial stochastic May–Leonard model where the conservation law for the total particle number has been removed, and where the mean-field dynamics is *not* characterized by neutrally stable orbits [13, 25, 39, 75]. To this end, we introduce quenched spatial disorder by treating the rate on each site of the lattice as a random variable drawn from a truncated Gaussian distribution. As shown in the snapshots in the second row of Fig. 3.1(compare with Fig. 3.1b), the presence of spatial clustering can still be observed even though small noisy spiral structures dominate the system. Thus, the spatial disorder does not markedly affect the formation and occurrence of spiral patterns.

The third row of Fig. 3.1 shows snapshots of the system after removing either the two-particle exchange process (3.3) or pure nearest-neighbor hopping (3.4). When exchange processes are not allowed, see Figs. 3.1g and 3.1i, cluster formation is still observed, while the spiral waves become rather noisy, and it is worth noticing that one additional cluster type consisting of only empty sites appears in the system (discernible as black patches in Figs. 3.1g and 3.1i), with measurable consequences on physical observables, as will be discussed below. Moreover, in Fig. 3.1h where only exchange processes are allowed, the spiral pattern boundaries appear quite distinctly sharp, while the empty sites are randomly distributed rather than clustered.

From these results, we infer that the formation of the observed spiral patterns is promoted by pair exchange processes. Furthermore, we have also verified that the above scenario is not affected when the rates are randomly distributed and therefore remains robust against spatial variability of the reaction rates.

3.2.2 Time evolution and spatio-temporal correlation functions

In order to quantitatively characterize the properties of the system, the influence of quenched spatial disorder, and the effect of pure particle pair exchange processes on the evolution of system, we next depict the temporal evolution of population density $a(t) = \langle n_A(j,t) \rangle$, the

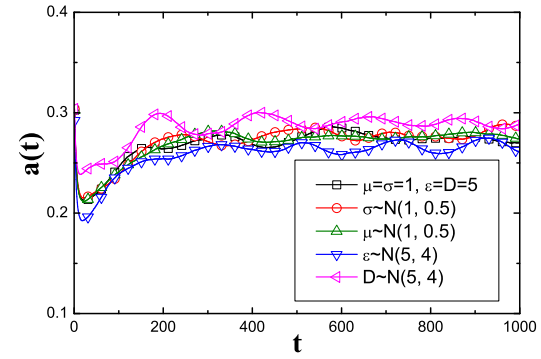

(a) Temporal evolution $a(t)$.

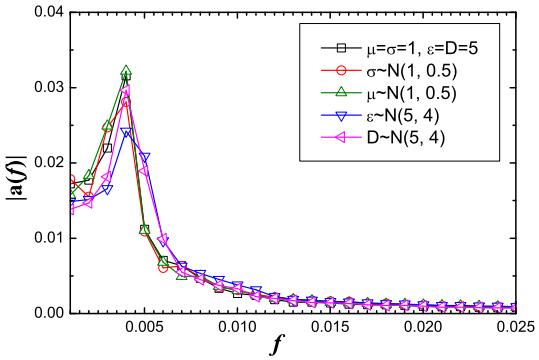

(b) Fourier transform $|a(f)|$.

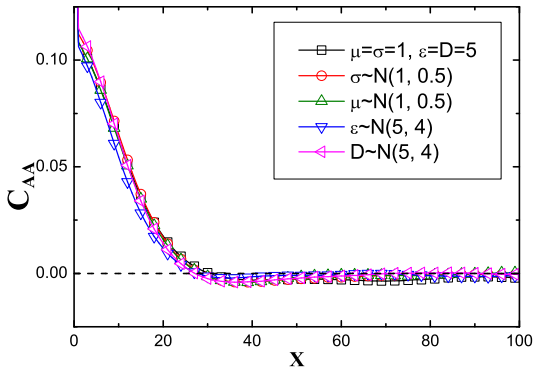

(c) Correlation function $C_{AA}(x)$.

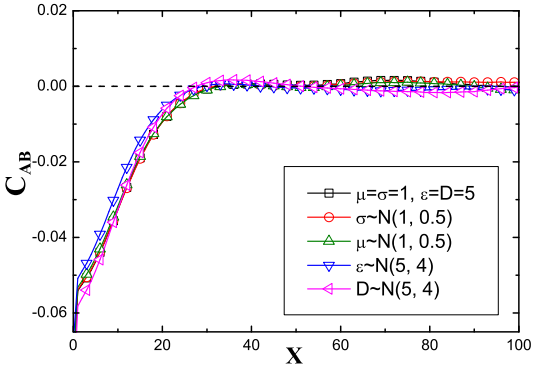

(d) Cross-correlation $C_{AB}(x)$.

Figure 3.2: Quantitative observables for a stochastic May–Leonard system with $N = 256 \times 256$ sites, starting with equal initial densities $a(0) = b(0) = c(0) = 1/3$ and in the presence of spatial disorder, averaged over 50 simulation runs. If unspecified, the default rate values $\mu = \sigma = 1$, $\epsilon = D = 5$ were used. The correlation functions in (c) and (d) were measured at $t = 1000$ MCS.

associated Fourier transforms $a(f)$, and the spatial auto- and cross-correlation functions C_{AA} and C_{AB}, respectively, in the quasi-stationary state (here, at time 1000 MCS) in Fig. 3.2. Since the reaction processes are symmetric with respect to the three species, the quantities associated with species A suffice to extract the relevant information for all three species. As shown in Fig. 3.2a, the population density decreases swiftly at the beginning of the simulation runs: as the particles are initially randomly distributed and fill the entire lattice, predation reactions (3.1) dominate and deplete the particle density at the beginning. However, with the emergence of spiral patterns, these reactions can only take place along the domain boundaries

of distinct species. The system then evolves towards the (quasi-)steady state with population densities ≈ 0.26 for the set of rates chosen here, consistent with the mean-field prediction $a^* = \frac{\mu}{3\mu+\sigma} = 0.25$.

In Fig. 3.2b, we depict the amplitude of the Fourier signal of the population density. The peak in $|a(f)|$ yields a characteristic oscillation frequency ≈ 0.004. This is almost a factor ten smaller than the prediction from the mean-field approximation, $f = \omega/2\pi = \sqrt{3}/16\pi \approx 0.034$, indicating a strong downward renormalization as consequence of spatial fluctuations and correlations, similar to the situation in the stochastic Lotka–Volterra model [46, 47] but in stark constract with the conserved spatially extended RPS model [3]. The finite width of the frequency peak in the Fourier plot indicates that the population oscillations will decay and ultimately cease after a finite relaxation time, consistent with the damped density fluctuations visible in Fig. 3.2a. Therefore, in the coexistence phase, the system's dynamics is consistent with the mean-field description, a feature that is however caused by the important influence of the particles' spatial mobility: With relatively low but still effective (average) mobility rates (on average $\epsilon = D = 5$), the dynamics of the system is dominated by local interactions (reproduction and predation) along the boundaries of local spiral clusters. Thereby, the coexistence state is maintained for a very long time and simultaneously effective mobility mixes the system well, resulting in a remarkably faithful description of the system through the mean-field approximation. Furthermore, the (quasi-) stationary auto- and cross-correlation functions in Figs. 3.2c and 3.2d decrease from their extremal values at vanishing distance to zero within about $\ell = 20$ lattice sites.

More importantly, Fig. 3.2 shows the influence of spatial disorder on the physical quantities in the May–Leonard system. We find that quenched randomness in the rates does not noticeably affect the temporal evolution of the population densities, the associated Fourier transform signals, or the decay lengths of the auto- and cross-correlation functions, irrespective of which rate is taken as random variable. This result demonstrates that our previous observation in the four-state RPS model with conservation law, where we found spatial disorder to have only minor effects, is also valid for the three-species May–Leonard system. Therefore, we conclude that predator–prey systems with cyclic competition appear to be generically robust against random spatial variations in the predation, proliferation, or mobility rates.

As demonstrated in Fig. 3.3, the formation of cluster patterns (see the third row of Fig. 3.1) ultimately renders the various observables qualitatively similar to those systems in which particles can move only via exchange processes. However, in Fig. 3.3 we also observe that the spatially averaged (quasi-)stationary density a^* and the peak in the Fourier transform $|a(f)|$ vary according to the degree to which nearest-neighbor hopping is included in the model. In particular, when particle dispersal happens solely through hopping processes (3.4), the asymptotic species densities are relatively low, see Fig. 3.3a with $\epsilon = 0$, $D = 5$; compare with the two plots for other rate choices, and the corresponding snapshots 3.1b, 3.1g, and 3.1h. We attribute this lower overall species fitness to the previously noted emergence of sizable clusters of just empty lattice sites in the absence of pair exchange processes (3.3), visible as small black patches in Figs. 3.1g and 3.1i. In fact, these voids effectively buffer

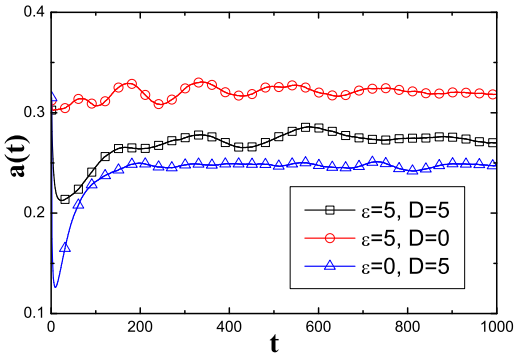

(a) Temporal evolution $a(t)$.

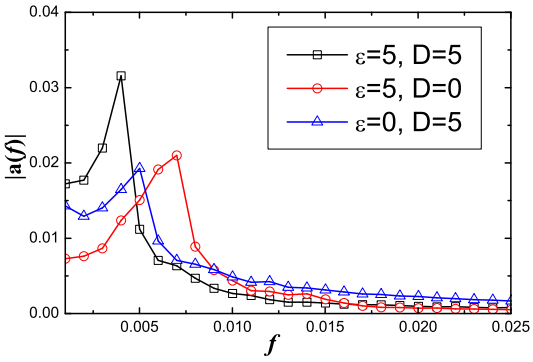

(b) Fourier transform $|a(f)|$.

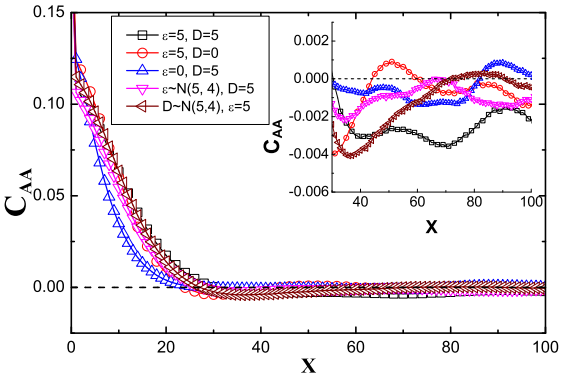

(c) Correction function $C_{AA}(x)$.

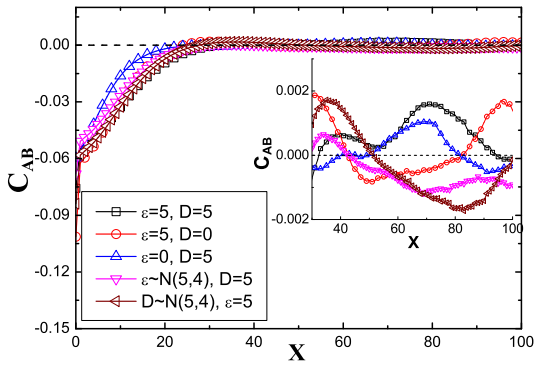

(d) Cross-correlation $C_{AB}(x)$.

Figure 3.3: Quantitative observables for a stochastic May–Leonard system with $N = 256 \times 256$ sites, reaction rates $\mu = \sigma = 1$, and starting with equal initial densities $a(0) = b(0) = c(0) = 1/3$, with different combinations of nearest-neighbor particle exchange and hopping processes, averaged over 50 simulation runs. The correlation functions in (c) and (d) were measured at $t = 1000$ MCS.

the three species against the predation reactions (3.1), but also diminish the total area that can be saturated by either population, which results in an overall density reduction in the (quasi-)steady state. In contrast, when particle pair exchange processes are included, the influence of empty-site clusters is diminished and consequently the (quasi-)stationary population densities enhanced (see Fig. 3.3a for $\epsilon \neq 0$). Furthermore, we observe that the characteristic density Fourier peak frequencies in systems where nearest-neighbor hopping is allowed are renormalized to even lower values than in runs with just pair exchange processes, which tend to better mix the system, see Fig. 3.3b (compare the characteristic frequency for

the runs with $D = 5$ to those with $D = 0$). In Figs. 3.3c and 3.3d, we observe the presence of low-amplitude population (damped) oscillations during the decay of the correlation function, which originate from the spiral structures displayed by the system in the coexistence state (under "efficient" mobility rates) [40]. In the insets of Figs. 3.3c and 3.3d, we notice that the correlation functions of the model variants with only hopping processes ($\epsilon = 0$) decay to zero in a less oscillatory manner than the correlation functions for the variants that include particle exchange ($\epsilon \neq 0$). This is a consequence of the observed absence of well-defined spiral structures (see Figs. 3.1g and 3.1i) when the pair-exchange rate is too low to efficiently stir the system.

In summary, the pair-exchange processes suppress the presence of empty-site clusters, and despite rendering the spiral structures more diffuse (i.e., more "entangled"), they have an overall stabilizing effect on emerging spatial patterns, and consequently promote the fitness and coexistence of all three subpopulations A, B and C.

3.2.3 Mean extinction times and their distribution

As we have discussed above, the system is efficiently stirred when the pair exchange rate ϵ is high enough (independent of the actual value of D). In this case, the system is characterized by a long-lived coexistence state. However, when the pair exchange rate is above some critical value, it has been shown that the system settles in an absorbing state after an observable amount of time [37]. We here revisit and extend the analysis of such a scenario that holds true for any values of ϵ or D by computing the mean extinction time (MET) and the distribution of extinction times. Here, for the sake of simplicity (and without loss of generality) we assume that $\epsilon = D$ and the mobility rate therefore is $M = 2\epsilon/N$. In this setting, our May–Leonard model coincides with the variant considered in Refs. [37, 38, 40], where it was shown that the critical mobility threshold is $M_c \approx 4.5 \times 10^{-4}$ (when $\mu = \sigma = 1$). Indeed, when the effective mobility rate M approaches M_c from below, there is a cross-over from a coexistence (quasi-)steady state to an absorbing state.

The MET has been computed as the time when the first of the three species dies out. Figure 3.4 illustrates how this MET exhibits markedly different behavior when the effective mobility rate $M = 2\epsilon/N$ is swept through M_c. As shown in Fig. 3.4b, when the mobility is relatively weak ($M = 10^{-6}$), the MET increases with the system size approximately according to the (zero-dimensional) functional form $\bar{T}_{\rm ex}(N) \sim e^{{\rm c}N}/N$ (where c is a constant) [17], especially for comparatively large values $N \sim 200 \ldots 600$. (For smaller systems with $N < 200$, the data do not fit this functional dependence very well, but may also not be as statistically reliable.) Yet the curvature of the graphs in Fig. 3.4a decreases upon raising the effective mobility, and the functional dependence on system size becomes replaced with a linear form $\bar{T}_{\rm ex}(N) \sim N$ for $M > M_c$. That is, when the mobility rate is low, the system is dominated by local interactions and species extinction is a rare event driven by a large fluctuation after an enormous amount of time. In this case, the coexistence of the

three species corresponds to a metastable state. Interestingly, Fig. 3.4c shows that spatial disorder in the mobility rate M does not qualitatively affect the behavior of the MET: this very same scenario applies even when M is randomly distributed. This observation further supports the conclusion that spatial variability in the mobility rates has little effect on the dynamical evolution of the system.

When the mobility rate increases and exceeds the threshold, the system is regularly driven towards extinction and biodiversity is lost, just as predicted by the zero-dimensional formulation of the model. Furthermore, the histograms of extinction times plotted in Figs. 3.4d and 3.4e show that the extinction time distributions (obtained for small systems with $N = 20 \times 20$ sites) correspondingly evolve gradually from an approximately exponential (or Poisson) shape, albeit with fat tails, towards a (roughly) Gaussian distribution centered at $\bar{T}_{\rm ex}$. In addition, the distributions remain unchanged even if spatial disorder is incorporated in the model (see the insets of Figs. 3.4d and 3.4e). The approximate quasi-exponential (or quasi-Poisson) distribution of Fig. 3.4d is a characteristic feature of systems where extreme events occur only after a very long time, and which are hence driven by large rare fluctuations [82]. Here, the rare extreme event is extinction of species that were previously coexisting in a metastable state for a long time period. On the other hand, the approximately Gaussian distribution of Fig. 3.4e is typical of systems where random fluctuations are of weak intensity [83]. In our competing three-species system, it is associated with the absorbing state that corresponds to species extinction happening within an "observable" time range, as in the zero-dimensional counterpart of the model [37, 38, 40]. These numerical observations support the method suggested in Ref. [37] for identifying the nature of (quasi-)steady states in the simulation of RPS models: A reasonable criterion is that the system remains at the steady state if three species still coexist after simulation time $t \sim N$, otherwise, the system evolves to an absorbing state.

3.3 Summary

In this chapter, we have demonstrated that quenched spatial disorder in either the reaction or the mobility rates does not significantly affect the temporal evolution, Fourier signals, spatial correlation functions, or mean extinction times in stochastic spatial May–Leonard models (i.e., four-state RPS models without total particle number conservation) in two dimensions. In combination with our previous results for conserved three-species RPS systems [3], we conclude that such cyclic predator-prey systems appear to be generically robust against spatial variability of the rates. Here, the randomized reaction rates remain attached to the lattice sites, mimicking environmental variations that do not change over time. As there exist a number of systems, e.g. in ecology [18] and microbiology [20], where the competition among species is cyclic, an important implication of our findings is that the environmental variability of the parameters can essentially be neglected in the mathematical description of those systems. In addition, through removing the hopping process by letting $D = 0$, we

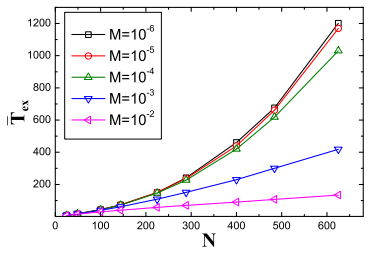

(a) $\bar{T}_{\rm ex}$ vs. N.

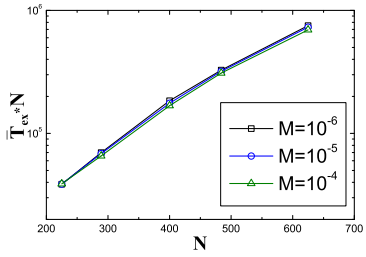

(b) $\log_{10}(\bar{T}_{\rm ex} \times N)$ vs. N.

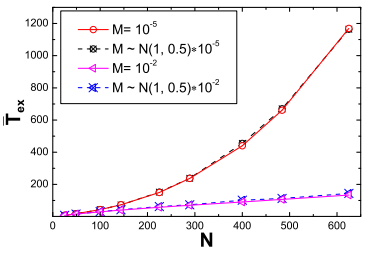

(c) $\bar{T}_{\rm ex}$ vs. N.

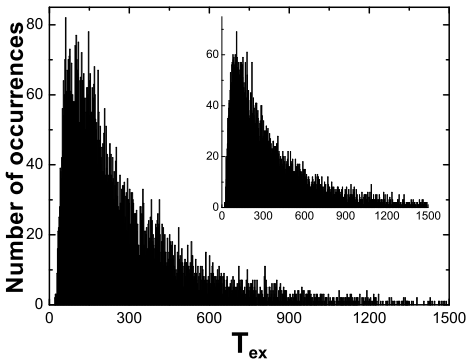

(d) $\epsilon = D = 0.1$; inset: $\epsilon = D \sim N(0.1, 0.05)$.

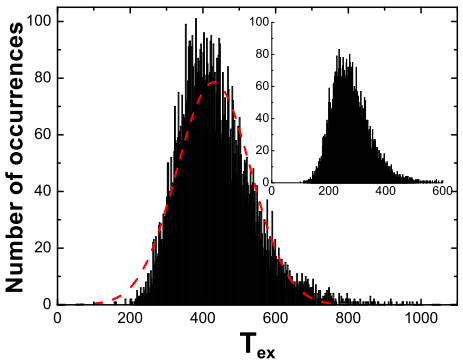

(e) $\epsilon = D = 25$; inset: $\epsilon = D \sim N(25, 10)$. The dashed (red/gray) curve depicts a Gaussian fit.

Figure 3.4: (a), (b), (c) Mean extinction time (MET) $\bar{T}_{\rm ex}$ as function of lattice size N, for different values of the effective mobility $M = 2\epsilon/N$ (here, $\epsilon = D$), obtained from averages over 10000 Monte Carlo runs, starting with equal initial densities $a(0) = b(0) = c(0) = 1/3$, and reaction rates $\mu = \sigma = 1$. The lattice sizes are $N = 5\times5$, 7×7, 10×10, 12×12, 15×15, 17×17, 20×20, 22×22, 25×25 sites. (d) and (e): Histogram of extinction times estimated from 10000 Monte Carlo runs, based on a system with lattice size $N = 20 \times 20$. The insets correspond to the histograms obtained for random mobility rates: $\epsilon = D \sim N(0.1, 0.05)$ in (d) and $\epsilon = D \sim N(25, 10)$ in (e).

observe that particle pair exchange processes promote the formation of sharp spiral patterns. In our spatial stochastic system, we measure the population oscillation frequency to be much lower than predicted by the mean-field rate equations, similar to the situation in two-species Lotka–Volterra models [46, 47], but in stark contrast with our numerical results for conserved RPS model variants [3]. This downward frequency renormalization is enhanced by the presence of nearest-neighbor hopping processes. Moreover, we find a remarkable gradual transformation in the dependence of the mean extinction time on system size, and the shape of the associated extinction time distribution, when the effective mobility rate crosses the critical threshold separating the coexistence from the absorbing state: When the mobility rate is low, the distribution of extinction times is approximately exponential, and species coexistence corresponds to a long-lived metastable state. In this case extinction is driven by large, rare fluctuations and the mean extinction time essentially grows exponentially with the population size. Above the critical mobility threshold, the extinction times are approximately distributed according to a Gaussian. In this situation, the noise is of weak intensity and the mean extinction time grows linearly with the population size. Interestingly, we find that these results remain valid for both non-random as well as for randomly distributed mobility rates.

Chapter 4

On the relationship between cyclic and hierarchical three-species predator-prey systems and the two-species Lotka–Volterra model

This chapter is in preparation for publication [4]. In this chapter, we aim to clarify the relationship and connections between interacting three-species models and the classic two-species Lotka–Volterra (LV) model that entails predator-prey coexistence with long-lived population oscillations. To this end, we utilize mean-field theory and individual-based Monte Carlo simulations to explore the temporal evolution characteristics of two different interacting three-species predator-prey systems, namely: (1) a cyclic rock–paper–scissors (RPS) model with conserved total particle number but strongly asymmetric reaction rates that lets the system evolve towards one "corner" of configuration space; (2) a hierarchical "food chain" where an additional intermediate species is inserted between the predator and prey in the LV model. For the asymmetric cyclic model variant (1), we demonstrate that the evolutionary properties of both minority species in the (quasi-)steady state of this stochastic spatial three-species "corner" RPS model are well approximated by the two-species LV system, with its emerging characteristic features of localized population clustering, persistent oscillatory dynamics, correlated spatio-temporal patterns, and fitness enhancement through quenched spatial disorder in the predation rates. In contrast, we could not identify any regime where the hierarchical three-species model (2) would reduce to the two-species LV system. In the presence of pair exchange processes, the system remains essentially well-mixed, and we generally find the Monte Carlo simulation results for the spatially extended hierarchical model (2) to be consistent with the predictions from the corresponding mean-field rate equations. If spreading occurs only through nearest-neighbor hopping, small population clusters emerge; yet the requirement of an intermediate species cluster obviously disrupts spatio-temporal correlations between predator and prey, and correspondingly eliminates many of the intriguing

fluctuation phenomena that characterize the stochastic spatial LV system.

4.1 Strongly asymmetric "corner" RPS model and mean-field analysis

As described in (2.1), the rock–paper–scissors model (RPS) consists of three zero-sum predator-prey interactions [13]. In our lattice Monte Carlo simulations we shall allow for nearest-neighbor exchange processes $X + Y \to Y + X$ with $X, Y \in (A, B, C)$. We also impose the constraint that at most a single particle (of either species) is allowed on each lattice site to mimic limited local carrying capacities that result from limited natural resources. In this present study, the total population density is always set to 1, and the lattice is hence fully occupied.

Within the mean-field approximation, the RPS system possesses a three-species coexistence state $(a^*, b^*, c^*) = \rho(\sigma, \mu, \lambda)/\,(\sigma+\mu+\lambda)$ (see (2.2); here, we use λ, σ, μ to label the corresponding reaction rates to resemble the notation used in the two-species LV model [46, 47, 48]), where $\rho = a(t) + b(t) + c(t)$ denotes the conserved total particle density [3, 26] (with $\rho = 1$ in this study). The three absorbing states $(\rho, 0, 0)$, $(0, \rho, 0)$, and $(0, 0, \rho)$ are all unstable in the mean-field approximation, but one of them will be eventually reached in any finite stochastic system, after a characteristic extinction time that increases exponentially with system size [3, 37, 40]. In our simulations, we employ sufficiently large lattices that extinction events are extremely unlikely within the run times. Therefore, systems with comparable reaction rates $\lambda \sim \sigma \sim \mu$ approach a (quasi-)steady state far away from the "corners" of configuration space. It has been demonstrated that stochastic fluctuations are comparatively small in such systems on two-dimensional lattices, and quenched spatial disorder in the rates has only minor influence on their dynamical evolution [3].

However, in the strongly asymmetric limit $\lambda \gg \sigma, \mu$, the mean-field stationary densities become to leading order $(a^*, b^*, c^*) \approx \rho\left(\frac{\sigma}{\lambda}, \frac{\mu}{\lambda}, 1 - \frac{\sigma+\mu}{\lambda}\right)$, and the corresponding fixed point moves to the vicinity of one of the corners of configuration space. Due to the relatively large reaction rate λ, species C acquires a very high population density (almost saturated, i.e., $c^* \approx \rho$) in the (quasi-)steady "corner" state. Since the C particles almost uniformly fill the lattice, the minority species A / B will essentially always encounter a nearest-neighbor partner C to undergo the third / second reaction in (2.1). The evolution of the rare species A and B in the RPS corner state can therefore be approximated by the following two-species Lotka–Volterra model reactions:

$$\begin{aligned} A \to &\quad \emptyset && \text{with rate } \hat{\mu} = \mu\, c^* \ ; \\ A + B \to &\quad A + A && \text{with rate } \lambda \ ; \\ B \to &\quad B + B && \text{with rate } \hat{\sigma} = \sigma\, c^* \ . \end{aligned} \tag{4.1}$$

Here, the symbol $\emptyset$ denotes the empty state. Notice that in this stochastic *effective* two-

species LV model on a lattice, empty sites inevitably appear in the system, no matter whether the lattice is initially fully occupied or not. In effect, the original exchange processes of minority A / B particles with the majority C species are replaced with nearest-neighbor hopping to empty sites in the resulting two-species LV model.

In the mean-field approximation, the LV model (4.1), with the constraint that at most one particle is permitted to reside on each site, is described by the following two coupled rate equations, where the total density ρ assumes the role of the overall carrying capacity [46, 49]:

$$\begin{aligned} \partial_t\, a(t) &= a(t)\,[\lambda\, b(t) - \hat{\mu}] \ , \\ \partial_t\, b(t) &= \hat{\sigma}\, b(t) \left[1 - \frac{a(t)+b(t)}{\rho}\right] - \lambda\, a(t) b(t) \ . \end{aligned} \tag{4.2}$$

These also follow directly from the RPS rate equations (2.2) by setting $c(t) \approx c^*$; more precisely, in the second rate equation for $b(t)$, employing the exact conservation relation $c(t) = \rho - a(t) - b(t)$ properly incorporates the limited local carrying capacities, and $\hat{\sigma} = \sigma\,\rho$. The stationary states of the coupled rate equations (4.2) consist of the linearly unstable extinction state $(a, b) = (0, 0)$, another absorbing state $(0, \rho)$ that is linearly stable for small $\lambda < \lambda_c = \hat{\mu}/\rho \approx \mu$, and the coexistence state $(a_s, b_s) = \left(\frac{\hat{\sigma}}{\hat{\sigma}+\lambda\rho}\left(\rho - \frac{\hat{\mu}}{\lambda}\right), \frac{\hat{\mu}}{\lambda}\right)$ that exists and becomes linearly stable if $\lambda > \lambda_c$. Therefore, in the thermodynamic limit the system displays a continuous non-equilibrium phase transition from an inactive, absorbing state to the active coexistence state at the critical predation rate λ_c. The universal power laws that emerge near the extinction threshold are characterized by the critical exponents of directed percolation [46, 53, 54, 84].

Linearizing around the active coexistence fixed point leads to

$$\begin{pmatrix} \partial_t\, \delta a \\ \partial_t\, \delta b \end{pmatrix} = L \begin{pmatrix} \delta a \\ \delta b \end{pmatrix} \ , \tag{4.3}$$

where $\delta a(t) = a(t) - a_s$ and $\delta b(t) = b(t) - b_s$, and with the linear stability matrix

$$L = \frac{1}{\lambda\rho(\lambda\rho + \hat{\sigma})} \begin{pmatrix} 0 & \lambda\rho\hat{\sigma}(\lambda\rho - \hat{\mu}) \\ -\hat{\mu}(\lambda\rho + \hat{\sigma})^2 & -\hat{\sigma}\hat{\mu}(\lambda\rho + \hat{\sigma}) \end{pmatrix} \ . \tag{4.4}$$

Its eigenvalues are

$$\epsilon_\pm = -\hat{\sigma}\hat{\mu}(2\lambda\rho)^{-1}[1 \pm \sqrt{1 - 4\lambda\rho\hat{\sigma}^{-1}(\lambda\rho\hat{\mu}^{-1} - 1)}] \ . \tag{4.5}$$

In the limit $\lambda \gg \sigma, \mu$ in the two-species LV model (4.1), we have $\lambda\rho\hat{\mu}^{-1} = \lambda\rho(\mu c^*)^{-1} \approx \lambda\mu^{-1} \gg 1$ and similarly, $\lambda\rho\hat{\sigma}^{-1} \gg 1$, whence the eigenvalues $\epsilon_\pm$ for the active coexistence fixed point turn into a complex conjugate pair with negative real part. This demonstrates that, in the strongly asymmetric limit $\lambda \gg \sigma, \mu$, the nature of the nontrivial coexistence fixed point is that of a linearly stable spiral singularity, and the (quasi-)steady state consequently is approached in an exponentially damped oscillatory manner. From the imaginary part

of the complex conjugate pair (4.5), we infer the characteristic oscillation frequency $f = \omega/(2\pi) \approx \sqrt{\hat{\sigma}\hat{\mu}}/(2\pi)$.

Moreover, there are two points worthwhile noticing:
(i) The strong asymmetry condition $\lambda \gg \mu, \sigma$ is the prerequisite for validating the approximative representation of the stochastic model (2.1) through the effective model (4.1); therefore, in the resulting two-species LV system (4.1) the predation rate λ is always larger than the critical threshold $\lambda_c = \mu c^*/\rho \ll \lambda$, and correspondingly the system resides deep in the active coexistence state.
(ii) When implementing the Monte Carlo algorithm for the effective model (4.1), instead of only introducing a local growth limit for the prey species B (which in the mean-field limit would be described by the rate equation $\partial_t\, b(t) = \hat{\sigma}\, b(t)[1 - b(t)/\rho] - \lambda\, a(t)b(t)$ [9, 47, 49]), we impose a maximum *total* population carrying capacity on each site in the simulation. Deep in the coexistence state, one would expect either variant to induce similar evolutionary dynamics for the model (4.1). First, since $\lambda \gg \sigma$, the stationary mean-field coexistence state concentrations for both model variants, namely with growth-limiting constraint on either the total or just the prey population, are essentially identical, i.e., $(a_s, b_s) \approx \left(\frac{\hat{\sigma}}{\lambda}\left(1 - \frac{\hat{\mu}}{\lambda\rho}\right), \frac{\hat{\mu}}{\lambda}\right)$. Second, we shall see that in our stochastic spatial simulations, the characteristic oscillation frequencies, which are inferred from the imaginary part of the eigenvalues $\epsilon_\pm$ in the nontrivial deep coexistence state, remain basically unchanged even if we only impose spatial occupancy restriction on the prey population [46, 47].

Altogether, it thus appears reasonable and legitimate on the ground of both mean-field theory and heuristic considerations that the stochastic spatial "corner" three-species RPS system approaches the two-species Lotka–Volterra model. In the following section, we shall demonstrate through detailed Monte Carlo simulations that this claim is valid.

4.2 Monte Carlo simulation results for the corner RPS and the associated LV models

We implement stochastic individual-based Monte Carlo simulations for both the "corner" RPS and the associated LV model on two-dimensional square lattices (typically with $N = 256 \times 256$ sites) with periodic boundary conditions according to the reaction schemes (2.1) and (4.1) that define these systems. The RPS model is moreover subject to nearest-neighbor exchange processes $X + Y \to Y + X$, where $X, Y \in (A, B, C)$, while in the LV system we also allow nearest-neighbor hopping $X + \emptyset \to \emptyset + X$, in addition to particle exchange. In either situation, a maximum occupancy of a single particle (of either species) is imposed on each lattice site to mimic a finite local carrying capacity resulting from limited natural resources. At each time step, one individual of any species is chosen at random, and simultaneously one of its four nearest neighbors (which might be an empty site in the LV system) is selected randomly. Subsequently, the center individual and its chosen neighbor undergo the various

reactions defined in the models according to the respective associated rates; otherwise, exchange (or hopping for LV) processes take place between the center particle and its chosen neighbor. Once on average all individual particles on the lattice have had a chance to be selected as center individual, one Monte Carlo step (mcs) is completed; therefore, the infinitesimal simulation time step is $\delta t \sim M^{-1}$, where M is the total number of individuals on the lattice present at that time (a fixed constant only for the RPS system). In the following, we are going to investigate four model variants:

1. "RPS" — "Corner" rock-paper-scissors model with strongly asymmetric rates, $\lambda \gg \sigma, \mu$, whence the system is thus going to eventually reach one of the corners of configuration space. In addition, we take the lattice for this model to always be fully occupied, $\rho = \rho(0) = 1$; therefore, only exchange processes take place in the simulation.

2. "RPS with disorder" — In order to study the effect of quenched spatial disorder, we will treat the predation rate λ at each lattice site as a random number drawn from a normalized Gaussian distribution truncated at one standard deviation on both sides: For example, $\lambda \sim N(m, n)$ implies that the predation rate λ is drawn from a truncated normal distribution on the interval $[m-n, m+n]$, centered at the value m with standard deviation $n < m$. In the simulation, the randomized rates are attached to each site (rather than to each individual), and held fixed (quenched) for a given disorder realization: The predation rates λ on all sites are determined at the beginning of each single Monte Carlo run, and remain unchanged until the next single run is initiated. Again, the total population density in the simulation is always set to $\rho = \rho(0) = 1$ and thus only exchange processes may take place. All other rates except λ stay the same as in the "RPS" models.

3. "LV" — Lotka–Volterra model with rates that originate from the rates in the corresponding corner RPS system: If rates λ, σ, μ are used in the RPS model, in order to appropriately compare the numerical results for both systems, we take $\lambda, \hat{\sigma} = \sigma c^*_{\rm mf}$, $\hat{\mu} = \mu c^*_{\rm mf}$ for the associated LV model, where $c^*_{\rm mf}$ represents the *mean-field* population density for the majority species C in the (quasi-)steady state in the asymmetric corner RPS model, as determined from the stationary solutions to the rate equations (2.2). Due to the lack of conservation law for overall population density, empty sites inevitably occur in the course of the simulation runs, and nearest-neighbor hopping also takes place in the simulation as well as exchange processes.

4. "LV with disorder" — We treat the predation rate λ at each lattice as a quenched random variable drawn from the same truncated normalized Gaussian distribution as in "RPS with disorder". Meanwhile, all other rates remain the same as those in the "LV" models, and again both exchange and hopping processes may take place in this system.

Typically, in order to study the connection between the corner RPS and its associated effective LV model, we shall numerically investigate their emerging spatio-temporal structures through instantaneous snapshots of the particle distribution on the lattice, the temporal evolution of the (spatially averaged) population densities, e.g., for species A, $a(t)$ and its associated Fourier transform $a(f)$ (see the definition in (2.5)), and the equal-time two-point

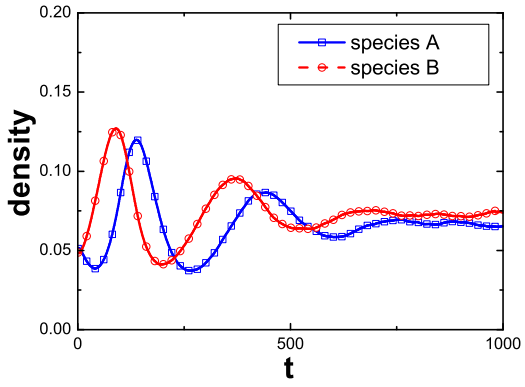

(a) minority population densities.

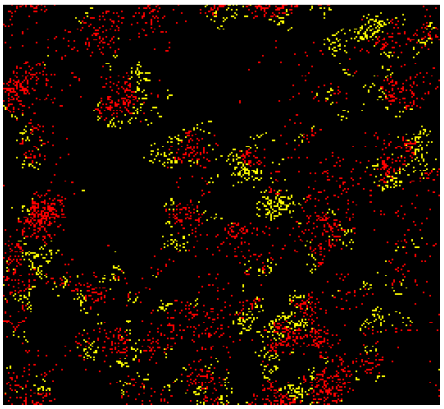

(b) lattice snapshot at $t = 1000$ mcs.

Figure 4.1: (a) Temporal evolution for the population densities of minority species A and B for an asymmetric RPS system with rates $\lambda = 0.8$ and $\sigma = \mu = 0.07$ on a square lattice with $N = 256 \times 256$ sites, periodic boundary conditions, and initial densities $a(0) = b(0) = 0.05$, $c(0) = 0.9$; the data are averaged over 50 simulation runs. (b) Corresponding snapshot of the spatial particle distribution at $t = 1000$ mcs (blue/dark gray: A, red/gray: B, black: C); note that there is no empty site in the lattice, since $\rho = a(0) + b(0) + c(0) = 1$ is conserved under the temporal evolution.

correlation functions in the (quasi-)steady state, for example $C_{AB}(x,t)$ (see the definition in (2.6)).

4.2.1 Self-organization in the coexistence phase of the two minority species in the corner RPS model

In Fig. 4.1a, the population densities for the minority species A/B in an asymmetric "corner" RPS system model on a square lattice with rates $\lambda = 0.8$ and $\sigma = \mu = 0.07$ are plotted as functions of simulation time t (in mcs). While the population densities for species A/B as obtained from the mean-field approximation for the RPS model would be identical, $\frac{\rho}{\lambda+\sigma+\mu}(\sigma,\ \mu) \approx (0.074,\ 0.074)$, the corresponding population densities in the associated LV model assume unequal values, $(a_s, b_s) = (0.065, 0.075)$ in the (quasi-)steady state. The LV predictions are remarkably close to the measured values $(0.064 \pm 0.003, 0.074 \pm 0.002)$ at long times in our Monte Carlo simulations, clearly distinct for species A and B. In particular, the persistent unequal population densities (starting from $t \approx 600$ mcs in Fig. 4.1a) support the population density inequality for minority species A/B in the (quasi-)steady state as statistically reliable. At the beginning of the simulations, we observe marked population oscillations, see Fig. 4.1a, reflecting the formation of complex spatio-temporal structures,

i.e., expanding activity fronts as familiar in the stochastic spatial LV system, noticeable as minority species clusters in Fig. 4.1b. The emergence of such localized species clusters promotes species coexistence, reduces the oscillation amplitudes in the system, and eventually allows the system to evolve into the (quasi-)steady coexistence state. In light of these observations, we conclude that the temporal evolution of the two minority species A/B in the stochastic spatial corner RPS model with strongly asymmetric rates can indeed be faithfully approximated by the predator–prey behavior in the related two-species LV model. We shall further support this assertion through additional observations in the following subsection.

4.2.2 Fitness enhancement of the minority species due to spatial variability in the corner RPS model

In order to further and quantitatively characterize the connection between the strongly asymmetric corner RPS system and its corresponding effective LV model, we next study the influence of quenched spatial disorder on the evolution of either system. Since spatial variability turns out to have very similar effects on species A and B, we mainly show the results associated with species A; a complete listing of data for characteristic observables is provided in Table 4.1. We depict the temporal evolution of the population density $a(t) = \langle n_A(j,t)\rangle$, its Fourier transform $a(f)$, and the spatial auto- and cross-correlation functions C_{AA} and C_{AB}, respectively, in the (quasi-)steady state (here, obtained at $t = 3000$ mcs) in Fig. 4.2. The default rates are set to $\lambda = 0.5$, $\sigma = \mu = 0.03$ in the corner RPS model, and correspondingly $\lambda = 0.5$, $\hat{\sigma} = \hat{\mu} = 0.027$ in the associated LV model, and $\lambda \sim N(0.5,\ 0.4)$ in both corner RPS and LV systems with quenched spatial disorder in the rate λ. Note that within the mean-field approximation, the population density for species A in the (quasi-) steady state is $a_s \approx 0.048$, and the characteristic critical predation rate threshold is $\lambda_c = 0.027 < \lambda$, guaranteeing that the associated LV system is located in the active (quasi-)steady coexistence region of the phase diagram; it is also worth noticing that the minimum predation rate in the model variants with quenched spatial disorder is 0.1, which is still well above the critical threshold, eliminating the possibility of any species extinction in our large lattices, even in the presence of spatial rate variability.

Figure 4.2a shows the simulated average population densities as function of time for the minority species A in both corner RPS and associated LV systems, in the absence and presence of quenched spatial disorder. In the (quasi-)steady state, the A species concentrations become 0.057 for the corner RPS model, 0.060 for the associated LV model, 0.063 for the RPS model with quenched spatial disorder, and 0.068 for LV model with spatial disorder (see Table 4.1). Thus, within the error bars the population density (0.057) for species A in the "pure" corner RPS model coincides with the simulation result (0.060) for the associated stochastic spatial LV model. Moreover, we observe that spatial variability in the corner RPS model enhances the fitness of the minority species, as measured by the asymptotic stationary concentrations, by $\sim 11\%$. This fitness enhancement is in qualitative accord with

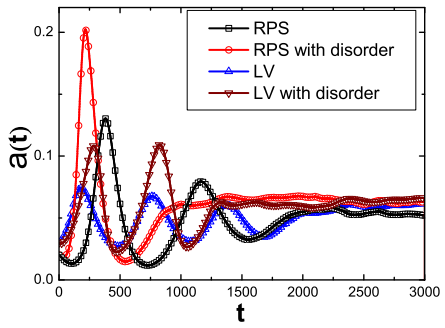

(a) Temporal evolution $a(t)$.

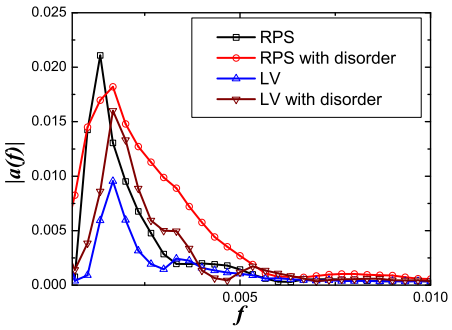

(b) Fourier transform $|a(f)|$.

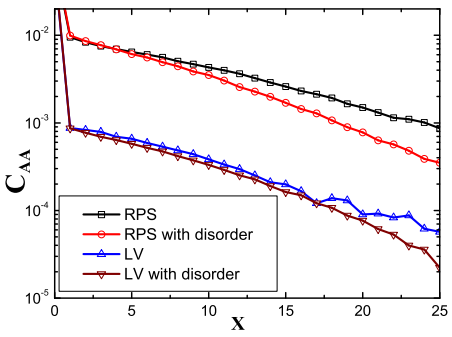

(c) Correlation function $C_{AA}(x)$.

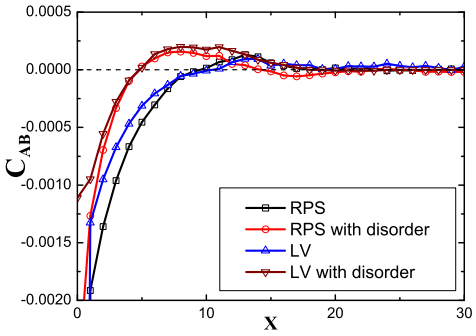

(d) Cross-correlation $C_{AB}(x)$.

Figure 4.2: Quantitative observables for a stochastic corner RPS model with rates $\lambda = 0.5$, $\sigma = \mu = 0.03$, and initial densities $a(0) = b(0) = 0.02$, $c(0) = 0.96$, and its corresponding LV system with $\lambda = 0.5$, $\hat{\sigma} = \hat{\mu} = 0.027$ and $a(0) = b(0) = 0.03$ from simulation runs on a square lattice with $N = 256 \times 256$ sites (periodic boundary conditions). In the presence of spatial disorder, $\lambda \sim N(0.5, 0.4)$. All simulation results were averaged over 50 runs, and the correlation functions in (c) and (d) were measured at $t = 3000$ MCS.

earlier investigations on the effect of quenched randomness in the predation rate for the the two-species LV model without site restriction [48], but turns out to be quantitatively less significant than the $\sim 25\%$ found there; it is also slightly smaller than the $\sim 13\%$ enhancement obtained directly in our simulations of the two-species LV model with restricted site occupation number, see Fig. 4.2a and Table 4.1.

We may attribute these differences to the fact that spatial disorder also affects the stationary population density c^* of the majority species C in the (quasi-)steady state of the corner RPS model, which in turn implies locally varying effective rates $\hat{\sigma}$ and $\hat{\mu}$ for the associated two-species LV model. This becomes apparent already on the mean-field description level, where

	a_s	b_s	$\tau_{A/B}$	l_{AA}	l_{BB}	l_{AB}
RPS model	0.057 ± 0.003	0.060 ± 0.002	~ 1800 mcs	13.2 ± 0.6	16.0 ± 2.0	~ 13.0
RPS with disorder	0.063 ± 0.002	0.067 ± 0.003	~ 800 mcs	9.4 ± 0.2	13.0 ± 1.0	~ 8.0
LV model	0.060 ± 0.003	0.063 ± 0.003	~ 2000 mcs	12.8 ± 0.5	15.5 ± 0.5	~ 13.0
LV with disorder	0.068 ± 0.002	0.070 ± 0.003	~ 1300 mcs	10.3 ± 0.3	11.2 ± 0.2	~ 9.0

Table 4.1: Characteristic physical quantities measured by Monte Carlo simulations for the four stochastic spatial RPS and LV models whose features are displayed in Fig. 4.2.

$c^* = \frac{\lambda}{\lambda+\sigma+\mu}$ and $\hat{\sigma} = \sigma c^*$, $\hat{\mu} = \mu c^*$. Then for the minority species concentration deep in the coexistence state of the corner RPS model one obtains $a_s \approx \frac{\hat{\sigma}}{\lambda} = \frac{\sigma}{\lambda+\sigma+\mu}$. Similarly, for the two-species LV model with site restrictions, $a_s \approx \frac{\sigma}{\lambda+\sigma}$, whereas $a_s = \frac{\sigma}{\lambda}$ in the LV model with infinite local carrying capacity. In the latter case, a broad distribution of predation rates λ strongly biases the system towards small values that considerably enhance the associated (quasi-)steady state density of A species [48]. For the RPS system or the LV model subject to site occupation restrictions, the additional rates in the denominators reduce the significance of this low-λ bias and ensuing concentration enhancement, and consequently the overall fitness enhancement is less pronounced.

As one would expect, the emergence of species clusters results in remarkable population oscillation at the beginning of the simulation runs, as seen in Fig. 4.2a. However, as shown in Fig. 4.2a, the transient period for the system evolving from the initial to the eventual active (quasi-)steady state is quite distinct for the different models. Correspondingly, the Fourier transformed density signal, which reflects both the characteristic oscillation frequency in the (quasi-)steady state and the associated characteristic relaxation time, is displayed in Fig. 4.2b. The Monte Carlo simulations exhibit the same peak frequency in the (quasi-)steady state for all four models, $f \approx 0.0014$; this characteristic peak frequency in the stochastic lattice systems is markedly reduced by $\sim 60\%$ as compared with the (linearized) mean-field prediction $f \approx \sqrt{\hat{\mu}\hat{\sigma}}/(2\pi) \approx 0.0043$. This remarkable decrease in typical population oscillation frequency can be attributed to the renormalization by stochastic fluctuation in the spatial system [46, 47, 84]. Moreover, the relaxation time $\tau = 1/\Gamma$, where Γ denotes the full width at half maximum of the oscillation peak in Fourier space, characterizes the typical time scale the system to relax towards the (quasi-)steady state, and thus it represents a measure of stability for these systems against external perturbations. Significantly, as demonstrated by the data in Fig. 4.2b and Table 4.1, the relaxation time in the RPS model with quenched spatial disorder is reduced by $\sim 50\%$ to ~ 800 mcs as compared with $\tau \sim 1800$ mcs in the corner RPS model without spatial rate variability.

The enhancement of both predator and prey fitness resulting from spatial variability in the stochastic lattice LV model is based on the emergence of more localized correlated spatio-temporal structures [48]. In all four model systems investigated here, such species clustering appears as well, see Fig. 4.1b. Compared to the RPS/LV model without spatial disorder,

the corresponding RPS/LV system with spatial variability in the reaction rate λ displays larger initial oscillation amplitudes (c.f. Fig. 4.2a), implying that spatial disorder in the predation rate tends to gather species closer, thus resulting in more localized and thus enhanced population growth spurts. To better understand the underlying spatial structures in our systems, we depict the static two-point auto-correlation functions in Fig. 4.2c and cross-correlation functions in the (quasi-)steady state in Fig. 4.2d. From these plots, we extract the typical correlation length l_{AA}, which measures the spatial extent of species A clusters by fitting the simulation data C_{AA} with an exponential function $exp(-|x|/l_{AA})$, and obtain the predator-prey separation length l_{AB}, defined as the location where C_{AB} assumes its maximum positive value. In the corner RPS model, the correlation and separation lengths turn out to be $l_{AA} = 13.2$ (in units of lattice spacing) and $l_{AB} = 13.0$, respectively, both of which coincide within the statistical error bars with the simulation results for the associated LV model, for which we find $l_{AA} = 12.8$ and $l_{AB} = 13.0$, as listed in Table 4.1. However, in the corresponding disordered RPS system, we measure markedly reduced values for the correlation and separation lengths, namely 9.4 and 8.0. This closer clustering near sites with locally favorable rates permits an overall larger number of population centers, and consequently enhances the net population densities for the minority species in the system with spatial variability in the rate λ.

In summary, as suggested on the basis of mean-field considerations, we find that the minority species A and B in our spatially extended stochastic RPS model with strongly asymmetric rates behave like the predator and prey in the coexistence phase of the two-species Lotka–Volterra model. Indeed, similar to our earlier findings for the lattice LV model [48], we observe that quenched spatial disorder can markedly enhance the fitness of both minority species. This feature distinguishes the corner RPS model from the perhaps more common RPS system with comparable reaction rates, whose stationary state resides close to the center of configuration space; in that situation, quenched spatial reaction rate disorder hardly influences the dynamical evolution of either species [2, 3].

4.3 The hierarchical three-species "food chain" model

In Section 4.2, we have demonstrated how the properties of the coexistence state in the two-species Lotka–Volterra model emerge as the rock–paper–scissors system is moved towards one of the corners of configuration space by choosing strongly asymmetric rates. Another natural idea to generate the LV model is to consider a hierarchical three-species "food chain" system, where an intermediate species C is inserted between the predators A and prey B. The question then becomes: Will a stochastic hierarchical three-species food chain model on a lattice in a certain limit again recover the properties of the spatial two-species LV system? To this end, we investigate the following coupled stochastic reactions that define

our three-species food chain:

$$\begin{aligned} A \to & \quad \emptyset & \text{with rate } \mu \ ; \\ A + C \to & \quad A + A & \text{with rate } \lambda \ ; \\ C + B \to & \quad C + C & \text{with rate } \lambda \ ; \\ B \to & \quad B + B & \text{with rate } \sigma \ . \end{aligned} \tag{4.6}$$

Species A and B in this model behave as predators and prey, respectively, while the intermediate population C preys on species B and is preyed upon by species A. In order to closely approach the two-species LV model and mainly study the dynamic behavior of predator A and prey B, in this food chain model we use the same predation rates λ for the AC and BC predation processes. In our Monte Carlo simulations for this spatially extended system on a square lattice with periodic boundary conditions, we allow at most one particle per site in the simulations. The resulting mean-field rate equations now read:

$$\begin{aligned} \partial_t \, a(t) &= a(t) \left[\lambda \, c(t) - \mu \right] \ , \\ \partial_t \, c(t) &= \lambda \, c(t) \left[b(t) - a(t) \right] \ , \\ \partial_t \, b(t) &= \sigma \, b(t) \left[1 - a(t) - b(t) - c(t) \right] - \lambda \, b(t) c(t) \ , \end{aligned} \tag{4.7}$$

since only the reproduction process for the species B requires the presence of an empty site in its immediate neighborhood, whereas newly generated A and C particles just replace their respective prey. As stationary solutions of the coupled rate equations (4.7), one finds one linearly unstable absorbing point $(a, c, b) = (0, 0, 1)$, an entire absorbing line $(0, c, 0)$, where $c \in [0, 1]$, and one active coexistence fixed point:

$$(a_s, c_s, b_s) = \left(\frac{\lambda\sigma - \mu(\lambda + \sigma)}{2\lambda\sigma} \ , \frac{\mu}{\lambda} \ , \frac{\lambda\sigma - \mu(\lambda + \sigma)}{2\lambda\sigma} \right) . \tag{4.8}$$

As in the two-species LV model with site occupation restrictions, there exists a critical threshold for the predation rate $\lambda_c = \frac{\mu\sigma}{\sigma - \mu}$ in this hierarchical food chain model, which represents the occurrence of a phase transition from the inactive absorbing states to the active coexistence state: When the predation rate is below the threshold ($\lambda < \lambda_c$), the system evolves towards extinction for the A and B population $(0, c, 0)$; otherwise, the system eventually reaches the three-species coexistence state (a_s, c_s, b_s). However, in stark contrast with the mean-field analysis for the two-species LV model with site restrictions, the population densities for the predators A and the prey B in this food chain system are always the same in the (quasi-)steady coexistence state, in order for the intermediate species C to possess a nonzero stationary population density. Other important distinct spatio-temporal properties for the spatially extended hierarchical food chain model will be discussed in the following two subsections.

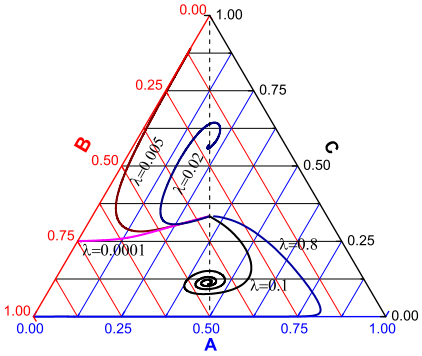

(a) normalized evolution trajectories

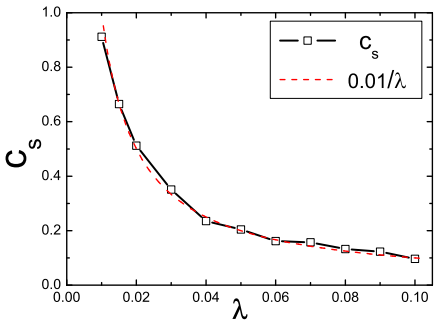

(b) $c_s \sim \lambda$ in (quasi-)steady state

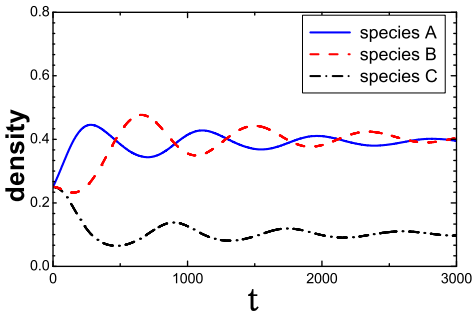

(c) population densities for $\lambda = 0.1$

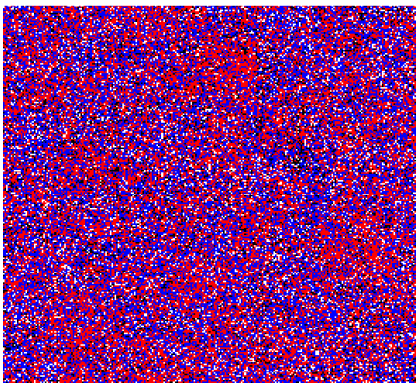

(d) snapshot for (c) at $t = 3000$ *mcs*

Figure 4.3: Quantitative observables for a stochastic three-species hierarchical food chain system with $N = 256 \times 256$ sites, reaction rates $\mu = 0.01, \sigma = 0.1$, starting with equal initial densities $a(0) = b(0) = c(0) = 1/3$ for models in (a) and (b), and $a(0) = b(0) = c(0) = 0.25$ for models in (c) and (d), averaged over 50 simulation runs. (d): blue/dark gray: A, red/gray: B, black: C, white: empty.

4.3.1 Mean-field behavior through both nearest-neighbor particle pair exchange and hopping processes

In the Monte Carlo simulation, we first permit both nearest-neighbor particle exchange and hopping processes to generate population spreading. In Fig. 4.3a, we depict the typical normalized trajectories for the population densities in the systems with various predation rates λ. Other rates ($\mu = 0.01, \sigma = 0.1$) in the systems remain unchanged, and thus the critical threshold value associated with predation rate is fixed $\lambda_c = \frac{\mu\sigma}{\sigma-\mu} \approx 0.011$. When the predation rate is below the threshold, the trajectories ($\lambda = 0.0001, 0.005$ in Fig. 4.3a) reach the boundaries of the phase graph, i.e., the systems evolve to the inactive absorbing states.

With the increase of predation rate ($\lambda = 0.02, 0.1$ in Fig. 4.3a), we observe that the system evolves to the active coexistence state. While for smaller values of predation rate ($\lambda = 0.02$ in Fig. 4.3a) the fixed point is a node, the typical spirals in phase graph appear for large values of predation rate ($\lambda = 0.1$ in Fig. 4.3a) and the associated fixed point becomes a focus. This point is similar to the situation in two-species LV model with site restriction [46]. As we discussed before, in active coexistence state predator A and prey B should possess the same population densities in order to let the intermediate species C also have nonzero stationary population density (see the dash line in Fig. 4.3a). However, with large predation rate λ relative to the rate μ ($\lambda = 0.8$ in Fig. 4.3a), the population density of intermediate species C in (quasi-)steady state is so small ($= \frac{\mu}{\lambda} \approx 0.01$) that the remarkable stochastic oscillation in the simulation causes the evolution trajectories to easily touch the boundary of the phase graph; thus, the system eventually stops at the absorbing states ($a,\ 0,\ b$) in the simulation which do not exist in mean-field analysis.

Furthermore, as shown in Fig. 4.3b, the quantitive relationship between the population density c_s for intermediate species C in active coexistence state and the predation rate λ numerically agrees with the mean-field analysis $c_s = \mu/\lambda$. In Fig. 4.3c, we plot the temporal evolution of species population densities for the model with predation rate $\lambda = 0.1$, the population densities in (quasi-)steady state are ($0.4 \pm 0.01,\ 0.1 \pm 0.003,\ 0.4 \pm 0.01$), fully consistent with the prediction in mean-field approximation. We also numerically investigate the influence of quenched spatial disorder on the dynamical evolution of the system. However, starkly in contrast with the finding of robust fitness enhancement in two-species LV model, in the hierarchical three-species model spatial variability on predation rate λ does not generate any remarkable effect on the dynamical evolution of the system. This point is further proved by the spatial distribution of particles on a two-dimensional lattice shown in Fig. 4.3d, where all particles are randomly distributed on the lattice in the (quasi-)steady state and robust spatio-temporal structures such as either clusters or spirals do not emerge in the system, thus the quenched spatial disorder can not greatly enhance the fitness of spatial systems.

At this point, we demonstrate that the spatial three-species hierarchical food chain system, extended through both nearest-neighbor particle pair exchange and hopping processes, can be well described by mean-field approximation. In the following subsection, we shall further demonstrate that particle pair exchange process alone can also purely well mix the system and make the system exhibit mean-field like behavior.

4.3.2 Particle pair exchange processes and pure hopping processes

In the above subsection, we have demonstrated that the population spreading processes, including both nearest-neighbor particle pair exchange and hopping processes, can well mix the two-dimensional spatially extended three-species hierarchical food chain system. In order to further explore the factor which accounts for the appearance of mean-field behavior, in Fig. 4.4a and 4.4b we show the snapshots of the systems within stationary states after

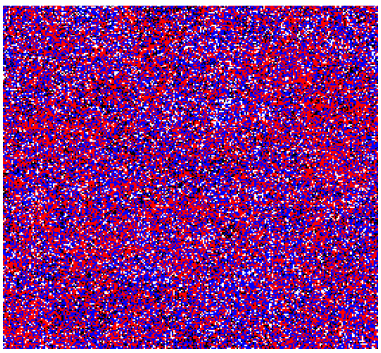

(a) particle pair exchange processes

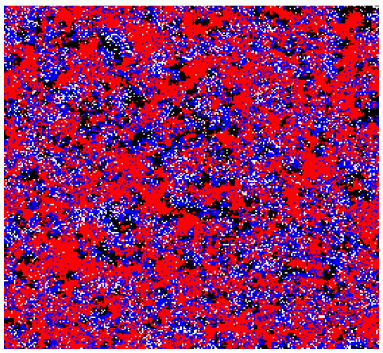

(b) pure hopping processes

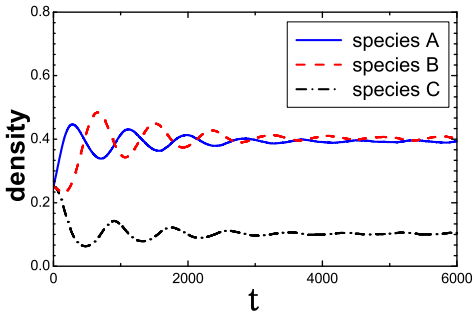

(c) Temporal evolution for (a)

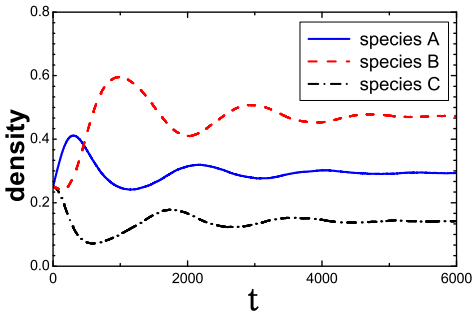

(d) Temporal evolution for (b)

Figure 4.4: (a) and (b): Snapshots of the spatial particle distribution at $t = 6000$ *mcs* for a stochastic three-species hierarchical food chain system with $N = 256 \times 256$ sites, reaction rates $\lambda = 0.1, \mu = 0.01, \sigma = 0.1$, starting with equal initial densities $a(0) = b(0) = c(0) = 0.25$. Blue/dark gray: A, red/gray: B, black: C, white: empty. (c) and (d): Temporal evolution of population densities for models described in (a) and (b), with $N = 100 \times 100$ sites, averaged over 50 simulation runs.

removing either the particle pair exchange process or pure nearest-neighbor hopping process. In Fig. 4.4a where only nearest-neighbor particle pair exchange process is allowed, it is shown that the individuals for each species are uniformly distributed on the lattice, and no particular spatial patterns emerge in the systems. Furthermore, we depict the associated temporal evolution (up to 6000 *mcs*) of population densities for a smaller system ($N = 100 \times 100$). As observed in above subsection, the population densities $(0.39 \pm 0.01, 0.10 \pm 0.01, 0.40 \pm 0.02)$ in (quasi-)steady states (at $t = 6000$ *mcs*) are still closely consistent with the mean-field predictions (see Fig. 4.4c) even though the nearest-neighbor particle hopping process has been removed from population spreading processes. Also, as we would expect (see the snapshot shown in Fig. 4.4a), in the simulation we do not observe remarkable influence of

quenched spatial disorder on the evolutionary dynamics of the system.

Moreover, we investigate the systems spatially extended only through nearest-neighbor hopping processes (see Fig. 4.4b and Fig. 4.4d). In Fig. 4.4b, species clusters emerge in the system as observed in two-species LV system; however, it is worthwhile noticing that the predation between predator A and prey B does not directly take place between their boundaries but indirectly be realized through the clusters of intermediate species C (see the black clusters in Fig. 4.4b). The presence of such intermediate species clusters significantly suppresses the effective indirectly reacting boundaries between predator A and prey B. Again, we find that quenched spatial disorder does not remarkably affect the evolutionary dynamics of the system. Meanwhile, as shown in Fig. 4.4d, the population densities $(0.29 \pm 0.01, 0.14 \pm 0.01, 0.47 \pm 0.02)$ in the (quasi-)steady state do not coincide with the predictions from mean-field rate equations, i.e., nearest-neighbor hopping processes alone are not strong enough to well mix the two-dimensional three-species hierarchical food chain systems. It is also worth mentioning that these numerical observations ($\lambda = 0.1$) about the effect of either particle pair exchange processes or pure hopping processes also apply to the systems with small predation rate (i.e., $\lambda = 0.02$).

In summary, the well-mixed hierarchical three-species food chain model with site restriction behaves as in the mean-field predictions. As observed in two-species LV system with site restriction, the hierarchical food chain model also possesses a critical threshold for predation rate, which characterizes a phase transition from inactive absorbing state to active coexistence state. We demonstrate that in coexistence state nearest-neighbor particle pair exchange processes effectively wash out the formation of species clusters and promote the appearance of mean-field like behavior. However, although species clusters emerge in the systems only with hopping processes, the appearance of intermediate species clusters suppresses the effective reacting boundaries between predator and prey so that the spatial variability still can not remarkably influence the dynamical evolution of food chain systems. That is, the hierarchical three-species food chain model is not closely similar to the two-species LV models.

4.4 Summary

In this chapter, we aim to study the connection between two interacting three-species models and the two-species Lotka–Volterra model. We study the evolutionary behavior of the two minority species in "corner" three-species rock–paper–scissors (RPS) model with strongly asymmetric rates. We analytically demonstrate that, in mean-field limit, the evolutionary dynamics of both minority species in "corner" RPS models can be well approximated by the two-species LV model. Then, within the Monte Carlo simulation for the "corner" RPS model, the population densities for those two minority species in (quasi-)steady state coincide with both the analytic predictions from mean-field approximation in the resulting two-species LV model and its associated numerical simulation results. Furthermore, through introducing

quenched spatial disorder into the predation rate λ in "corner" RPS model, we observe that the influence of quenched spatial disorder on the evolution of system can not be ignored any more (instead, in the RPS system far away from the "corner" of configuration space, quenched spatial disorder has minor effect on the evolution of system [3]), and the fitness of two minority species in the "corner" RPS system is remarkably enhanced due to the spatial variability on predation rate λ, i.e., larger population densities for both minority species in (quasi-)steady state, shorter relaxation time, and more localized clusters for those two minority species. That is, the two minority species in the "corner" RPS model behave like the predator and prey in the classic two-species LV models.

In addition, we investigate the hierarchical three-species "food chain" model, in which an additional intermediate species is inserted between the predator and prey in classic two-species LV model. As observed in the spatial version of two-species LV model with site occupancy restriction, in the carrying capacity-restricted version of three-species "food chain" model, there exists a critical threshold for predation rate, which represents a non-equilibrium phase transition from inactive absorbing state to active coexistence state; and meanwhile the simulation results show that nearest-neighbor particle pair exchange processes can well mix the systems, wash out the formation of species cluster so that such systems can be well approximated by mean-field rate equations and the influence of quenched spatial disorder can be ignored. Moreover, in the systems spatially extended only by nearest-neighbor hopping processes, species clusters appear in the coexistence state; however, due to the interruption of intermediate species clusters, the effective predation between predator and prey is suppressed, resulting in that the quenched spatial disorder still can not enhance the fitness of the predator and prey even though remarkable species clusters are observed as in two-species LV systems. That is, as opposed to the "corner" rock-paper-scissors model with strongly asymmetric rates, this hierarchical three-species "food chain" model actually does *not* behave like two-species LV model.

Chapter 5

Emergence of universal scaling in a single asset market

In many physical complex systems with large amount of interacting components, universal scaling properties such as power law have been widely observed. Significantly, in the empirical research on financial markets, the emergence of universal scaling such as fat-tail distributions of asset return and trading volume, and long-range correlation in volatility have been found. In this chapter, we present one heterogeneous interacting agent model to study the emergence of scaling behavior in the financial market. This agent model and its associated numerical and analytical results presented in this chapter have been studied and published by S. V. Vikram and S. Sinha in their paper [65]. Through Monte Carlo simulation on the heterogeneous interacting agent model, we demonstrate that the asset price can be a critical global variable to coordinate the actions of investors who are otherwise independent. Moreover, we numerically and analytically prove that the fat tail of trading volume distribution is responsible for the fat-tail nature of return distribution.

5.1 Heterogeneous interacting agents model (HIAM) for one single asset market

We assume that the market for the single asset consists of N agents/investors. For each agent i ($i = 1, ..., N$), there are three states at each time step, i.e., $S_i(t) =: 0$ (no trading), $+1$ (buy one share of the asset), and -1 (sell one share of the asset). For simplicity, one unit quantity of asset is traded for each investor if the investor trades at each time step. Actually, the distribution of trading volume at each time step is scaled proportionally even if more than one unit quantities of asset (such as ± 2) apply in the model. In addition, individual-based variability in trading quantities is not necessary because we shall attach the individual-based heterogeneity onto the sensitivities of agents to the asset price.

After all investors react to the market at each time step, the net demand on the asset is measured as $M_t = \frac{1}{N}\sum_i S_i(t)$ to update the subsequent asset price p_{t+1}, and the net demand M_t might be positive and negative ($M_t \in [-1, 1]$). When updating the asset price according to the net demand, there are several points we need to consider: (i), the asset price should always be nonnegative no matter how low the net demand on the asset is; (ii), the asset price should rise/decline if the net demand is positive/negative respectively; (iii) the asset price should remain unchanged if the net demand is 0 ($M_t = 0$), i.e., either all agents do not trade on the asset at this time step or the gross demand for the asset is perfectly balanced by the supply of the asset. Therefore, the quantitative relationship between net demand and asset price should be mapping the domain $[-1, 1]$ of net demand M_t to the domain $[0, +\infty)$ of asset price p_t. Correspondingly, the response function $p_{t+1} = [(1 + M_t)/(1 - M_t)]p_t$ is one of the appropriate choices to update the asset price according to the net demand at each time step.

The agents/investors make their decisions of buying/selling according to both the current asset price and their individual understanding of "true" asset value. In the efficient market assumption, while price fluctuations exist in the market, the asset price evolves around the true asset value, thus it is reasonable for investors to estimate the "true" asset value as the long-term average of observed price series [85]. That is, the "true" asset value p_t^* perceived by the investors is estimated as $p_t^* \approx < p_t >_\tau$, where τ is the duration of a moving time window used to measure the "true" asset value and $\tau = 10^3$ in our following simulation. In addition, if the whole duration of historical data is less than τ in the simulation, the "true" asset value is measured as averaging over all historical prices on hand. Based on the perceived "true" asset value and the current asset price, the investors/agents decide to either buy/sell one share of the asset or not trade on the asset at current time step. The probability of trading on the asset is [65]

$$Prob(|S_i(t)| = 1) = \exp(-\mu_i |\ln(\frac{p_t}{p_t^*})|) \tag{5.1}$$

where the parameter μ_i represents the sensitivity of the individual agent/investor i to the deviation of the current asset price from the "true" asset value. Due to the diversification of individual investors' investment experiences and education levels, the risk-aversion degrees are distinct for different agents/investors i.e., the sensitivity of agents/investors to market fluctuations (i.e., market risk) is individual-based heterogeneous. In our simulation, we shall treat the parameter μ_i as a random number drawn from a uniform distribution to mimic the heterogeneity of risk-aversion degree for individual agents/investors. After the agent/investor i has decided to trade on the asset, he still needs to make a decision on either buying or selling the asset. Note that, due to various available trading strategies and the use of complex financial derivatives in the market, one individual agent/investor does not necessarily either buy the asset when the current asset price is below the "true" asset value or otherwise sell the asset. In other words, the decision of buying/selling the asset can be treated as a random walk at each time step, and it is an appropriate assumption that each agent/investor either buys or sells the asset with equal probability, i.e., independent of the

price level and its associated fluctuation.

We have now described the main details of the heterogeneous interacting agent model; and the underlying economic understandings on the associated assumptions. The model can thus be summarized as follows:

$$\begin{aligned} S_i(t) &\in \{0,\ -1,\ +1\} \\ M_t &= \frac{1}{N}\sum_i S_i(t) \\ p_{t+1} &= [(1+M_t)/(1-M_t)]p_t \\ Prob(|S_i(t)|=1) &= \exp(-\mu_i|\ln(\frac{p_t}{p_t^*})|) \\ Prob(S_i(t)=+1) &= Prob(S_i(t)=-1) \end{aligned} \tag{5.2}$$

where i labels the agent/investor, $i = 1, ..., N$, $\mu_i \sim U[10, 200]$, and $p_t^* \approx\!< p_t >_\tau$ ($\tau = 10^3$ is the duration of the moving time window).

As we have discussed, we want to investigate the empirical phenomena appearing in the real market, such as, volatility clustering, the fat-tail distribution of return and trading volume, and long-range correlation in volatility. Therefore, we are going to study the temporal evolution of asset price p_t, its associated unnormalized returns R_t and normalized returns r_t, volatility σ_t (i.e., the standard deviation of normalized returns measured over a moving time window), trading volume n_t (i.e., the total number of investors who trade at time t), and the two-point autocorrelation functions $C(s)$ of the time series of returns r_t. The explicit expressions to numerically calculate the above quantities of interest are as follows:

$$\begin{aligned} R_t &= \ln(p_{t+1}) - \ln(p_t) = \ln\frac{p_{t+1}}{p_t} \\ r_t &= \frac{R_t - < R_t >}{\sigma_{R_t}} \\ \sigma_t &= \sqrt{\frac{1}{\tau-1}\sum_{j=1}^{\tau}(r_{t-j} - < r_t >_\tau)^2} \\ n_t &= \sum_i |S_i(t)| \\ C(s) &= \frac{1}{T-s-1} r_t r_{t+s} \end{aligned} \tag{5.3}$$

where $i = 1...N$, $t = 1...T$, and T is the duration of the whole simulation (i.e., the number of Monte Carlo simulation steps); note that the time series r_t has mean zero and volatility one, thus resulting in the above simplified form of autocorrelation function. Besides, in the simulation, once all agents/investors have been chosen to make a trading decision, one Monte Carlo step (mcs) is completed; therefore, the infinitesimal simulation time is $\delta t = N^{-1}$, where N is the number of agents/investors in the system.

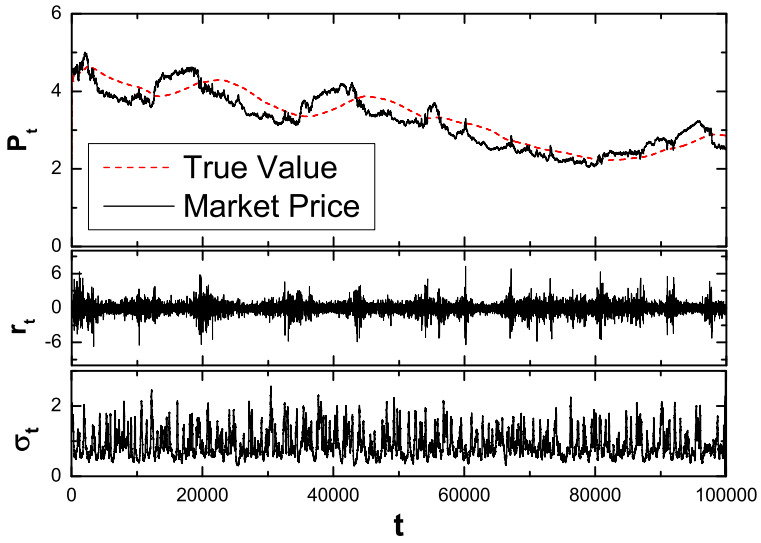

Figure 5.1: Temporal evolution of asset price p_t, normalized return r_t, and volatility σ_t. The default parameter values in the simulation are $T = 10^5$, $N = 10^5$, $\mu_i \sim U[10,\ 200]$, $\tau = 10^3$.

5.2 Monte Carlo simulation results for the heterogeneous interacting agents model

In Fig. 5.1, we plot the temporal evolution of asset price p_t and its associated "true" value, the evolution of normalized return r_t, and the evolution of volatility measured over the moving time window. First, the asset price p_t, the unsmooth line shown in the first row of Fig. 5.1, quantitatively tracks the underlying "true" asset value (smooth dashed/red line) observed by the agents/investors in the market. That is, although uncertainty in trading decisions of investors results in stochastic fluctuations of trading volume in the system, the heterogeneous interacting agents model can closely mimic the dynamical evolution of the market index, which is estimated as the average of historical asset prices and is perceived as "true" price by the investors. Second, it is shown that the normalized returns r_t exhibit significantly large fluctuation compared to the normal Gaussian noise (see the middle row of Fig. 5.1). Meanwhile, the bursts of large fluctuations have the tendency to occur together, a phenomenon called volatility clustering; this can be more clearly explained in the temporal evolution of volatility σ_t (the bottom row of Fig. 5.1).

The tradeoff relation between return and risk indicates that high risk (i.e., large fluctuations) must be paid off by high return on average. Therefore, the feature of volatility clustering

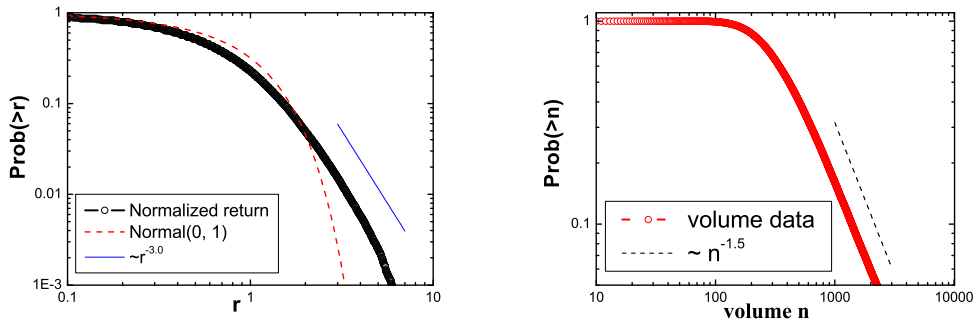

(a) cumulative distribution of normalized return (b) cumulative distribution of trading volume

Figure 5.2: Distributions of normalized returns r_t and trading volume n_t ($log_{10} \sim log_{10}$). The default parameter values in the simulation are $T = 10^5$, $N = 10^5$, $\mu_i \sim U[10,\ 200]$, $\tau = 10^3$. "Normal(0, 1)" in (a) represents the cumulative distribution for a normal Gaussian distribution with mean 0 and variance 1.

should be reflected in the returns, and thus it becomes significantly interesting to examine the distribution of returns. In Fig. 5.2a, the cumulative distribution $Prob(> r)$ for returns r_t displays a remarkable power-law tail with exponent ~ -3; this agrees with the results obtained from empirical daily data [69, 86]. In order to understand the emergence of the fat-tail distribution of returns, we shall further investigate the properties of trading volume which is the key to update the net demand and further adjust the market price of the asset. The trading volume is defined as the total number of agents/investors who trade at each time step, i.e., $n_t = \sum_i |S_i(t)|$. From Fig. 5.2b, we see that the distribution of trading volume also shows a heavy fat-tail with exponent ~ -1.5, which is almost identical to the observation in the real market [87]. This result is robust with regard to the number of units traded by the agents/investors at each time step: the fat-tail nature of trading volume remains unchanged even though we treat the number of units traded by the agents as a random number drawn from a Poisson distribution. In next section, we shall analytically demonstrate that the fat-tail nature of trading volume results in the associated power-law tail of the return distribution.

In Fig. 5.3, we turn to the correlation properties (see the definition for autocorrelation function $C(s)$ in (5.3)) of the return time series. It is shown that the autocorrelation of returns r_t oscillates around zero, i.e., r_t is uncorrelated, consistent with the interpretation from efficient market hypothesis. However, the time series of absolute values of returns $|r_t|$ shows a strong logarithmic decay with respect to the time lag in the autocorrelation function. Due to the fact that the absolute return r_t is one way to measure the return fluctuations, this logarithmic decay in autocorrelation of $|r_t|$ implies the long-memory property of volatility [88] (i.e., strong autocorrelation for the time series of variance). In other words, the influence

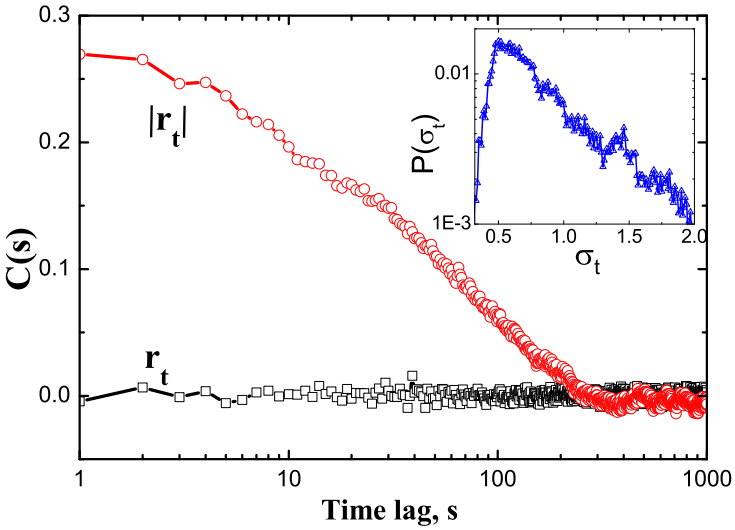

Figure 5.3: Autocorrelation functions of normalized return r_t and its absolute values $|r_t|$ (linear $\sim log_{10}$). (Inset) probability distribution of the volatility σ_t ($log_{10} \sim$ linear). The default parameter values in the simulation are $T = 10^5$, $N = 10^5$, $\mu_i \sim U[10,\ 200]$, $\tau = 10^3$.

of the emergence of big news in financial market usually lasts for a long time. In addition, in the inset of Fig. 5.3, it is shown that the volatility follows a log-normal distribution as observed in empirical markets [89].

5.3 Fat-tail distribution of returns is resulted from the fat-tail nature in trading volume distribution

As one would expect, the emergence of power-law properties in financial market is strongly related to the trading decisions made by the agents/investors; their decisions result in a stochastic trading volume at each time step. We have numerically shown that the distribution of trading volume also displays fat-tail features. The question is: is there any connection between the fat-tail property in the trading volume distribution and the emergence of power-law tail in returns? In order to answer the question, we let all agents/investors trade at each time step in the simulation (i.e., $n_t = N$ by letting $\mu_i = 0$) and then find that the fat-tail nature of return is absent. That is, indeed, the varying trading volume results in the fat-tail return distribution. As follows, we shall analytically interpret the relation between trading volume and return.

Due to the equal chance between buying and selling for each individual agent who trade at

each time step, we can treat each single update of asset price as the result of n_t steps of a symmetric random walk. Therefore, given constant trading volume ($n_t = n$, $n \in [1, N]$), the conditional return distribution $P(r|n)$ follows a normal Gaussian distribution with mean 0 and a variance proportional to trading volume n. Then, when varying the trading volume, we can express the return distribution $P(r)$ as the sum of conditional expectation over all possible trading volumes. This is expressed as follows,

$$\begin{aligned} P(r) &= \sum_{n=1}^{N} P(r|n)P(n) \\ &= \sum_{n=1}^{N} \frac{1}{\sqrt{2\pi n}} \exp(-r^2/2n)P(n) \end{aligned}$$

Based on the prior simulation result, the cumulative distribution of trading volume n has a fat tail with exponent ~ -1.5, thus the distribution $P(n)$ of trading volume has a tail with exponent ~ -2.5, i.e., $P(n) \sim n^{-2.5}$ for the tail of trading volume distribution. Then, the tail of the return distribution $P(r)$ now read:

$$\begin{aligned} P(r) &\sim \sum_{n=1}^{N} \exp(-r^2/2n)n^{-3} \\ &\sim K(2, 3, -r^2/2) \\ &\sim r^{-4}[2 - e^{-r^2}(2 + r^2)] \\ &\sim r^{-4} \end{aligned}$$

where $K(.)$ is the Kummer confluent hypergeometric function which can be evaluated numerically. Therefore, the return distribution $P(r)$ has a tail with exponent -4, indicating that the tail of cumulative distribution of returns follows a power law with exponent -3, completely agreeing with the prior simulation result and the observation in real markets [69, 86]. In all, both numerical simulation and probability analysis demonstrate that the fat-tail distribution of trading volume results in the associated fat-tail nature of the return distribution.

5.4 Summary

In this chapter, through Monte Carlo simulation, we show that our heterogeneous interacting agents model can mimic the universal scaling properties observed in real markets, such as, volatility clustering, power-law tail for both return distribution and trading volume distribution, and long-range memory of volatility. Significantly, it is numerically and analytically demonstrated that the emergence of fat tails in the return distribution is caused by the fat-tail distribution of trading volume. In addition, even though no direct interactions between

agents/investors exist in our model, the asset price behaves as a global variable to indirectly connect all agents together, causing the whole market to exhibit collective behavior such as universal scaling phenomena.

Chapter 6

Conclusion

6.1 Summary

As an important application of game theory to biological/physical systems with evolving populations/particles, evolutionary game theory has proved itself to be invaluable in explaining many complex systems in biology, economics, and other social sciences. In this dissertation, we employ techniques from statistical physics to investigate the spatial variants of several well-known games, particularly, the three-species cyclic competing rock–paper–scissors game either with or without conserved total population number, and a hierarchical three-species "food chain" model. Meanwhile, we study the connection between the two-species Lotka–Volterra predator-prey model and the three-species "corner" rock–paper–scissors game, and analytically and numerically demonstrate that the two-species predator-prey model is located at one of the "corners" of configuration space of three-species rock–paper–scissors systems. In addition, we also employ a heterogeneous interacting agent model [65] to study the emergence of universal scaling in financial markets.

First, in Chapter 2, through Monte Carlo simulation on two- and one-dimensional lattices with periodic boundary conditions, we investigate the influence of finite carrying capacity and spatial disorder in the reaction rates on the evolutionary dynamics of several variants of stochastic spatial rock–paper–scissors (RPS) models (with conserved total particle number). Particularly, the reaction rates in those model variants are comparable with each other so that the associated (quasi-)steady coexistence states are close to the central part of configuration space and correspondingly far away from the "corners". In two-dimensional versions, due to the conservation law of total particle number, not regular spiral patterns but species clusters emerge in the systems; and the systems can be well described by the mean-field approximation. It is shown that neither site occupation capacity restriction nor spatial variability in the reaction rates can remarkably influence the populations' temporal evolution, its associated characteristic oscillation frequency, or equal-time spatial correlation functions.

This is starkly different from the observations in the related two-species Lotka–Volterra predator-prey model, where quenched spatial disorder can remarkably enhance the fitness of both predator and prey. In one dimension, the systems with nearest-neighbor particle pair hopping processes are driven to extinction states, where only one single species survives, with the mean extinction time $T_{\rm ex} \sim N^{\gamma}$, $\gamma \approx 1 \ldots 1.8$. Meanwhile, in one-dimensional models either with or without finite carrying capacity, it is demonstrated that the single-species domains grow with a power law $\langle \lambda(t) \rangle \sim t^{3/4}$ as predicted in the references [29, 30].

Furthermore, in Chapter 3, we numerically studied the two-dimensional stochastic May–Leonard models (i.e., four-state RPS models without the conservation of total particle number). Again, it is shown that quenched spatial disorder in either the reaction or the mobility rates does not significantly influence the temporal evolution of population densities, its associated Fourier signals, equal-time spatial correlation functions, or mean extinction times. Therefore, together with the numerical results for conserved three-species RPS systems [3], it is demonstrated that the physical properties of such cyclic RPS systems (either with or without conservation law) are robust against quenched spatial disorder in the rates. This implies that the environmental heterogeneity in three-species cyclic competing systems can essentially be ignored when mathematically describing those systems. In addition, in the two-dimensional stochastic May–Leonard systems, we find that pure particle pair exchange processes can promote the forming of regular spiral patterns. Meanwhile, through Monte Carlo simulation on small two-dimensional May–Leonard systems, we show that, when the mobility rate crosses the critical threshold which separates the coexistence state from the absorbing states, there exists a gradual transformation in the dependence of the mean extinction time on system size and in the associated extinction time distributions. When the mobility rate is below the critical threshold value, the extinction time distribution is approximately exponential and the associated mean extinction time grows exponentially with the population size. However, when the mobility rate is above the critical mobility threshold, the extinction time distributions are approximately Gaussian-shape and the mean extinction time grows linearly with the population size.

Previous studies on rock–paper–scissors games (either with or without conserved total population number) focus on the metastable states around central part of the configuration space. Therefore, in Chapter 4, we switch our study to the "corner" rock–paper–scissors model with strongly asymmetric rates, which let the system evolve to the "corner" of configuration space. We mainly studied the evolutionary behavior of the two minor species in (quasi-) steady state in the "corner" rock–paper–scissors model. Through the mean-field rate equation approximation and Monte Carlo simulations, we analytically and numerically demonstrate that the two-species Lotka–Volterra model is one of the "corners" of configuration space in the three-species rock–paper–scissors model. As observed in two-species Lotka–Volterra models, we find that the influence of spatial variability of predation rate on the evolutionary dynamics of two minor species in the "corner" RPS system is sizeable, and the fitness of both minor species is remarkably enhanced owing to the presence of spatial variability on predation rate, i.e., larger population number in (quasi-)steady coexistence

state, shorter relaxation time, and more localized species clusters. Therefore, this finding provides us some insights into the physical connection between two-species reaction models and three-species cyclic competing models. In order to further explore this connection, we investigate a hierarchical three-species "food chain" model, in which an additional intermediate species is inserted between the predator and prey in two-species predator-prey model. Through Monte Carlo simulation on a two-dimensional lattice with at most one particle per site, we observe a critical threshold for predation rate in the well-mixed system. As observed in the two-species Lotka–Volterra model with finite site occupancy capacity, the threshold represents a continuous nonequilibrium phase transition from an inactive absorbing state to an active coexistence state. Moreover, we find that particle pair exchange processes can well mix the system such that no species clusters emerge in the (quasi-)steady states and further the dynamics of the system coincide with mean-field approximation. In addition, the presence of intermediate species interrupts the direct reactions between predator and prey in two-species Lotka–Volterra model; quenched spatial disorder does not significantly affect the evolutionary dynamics of (quasi-)predator and (quasi-)prey in the hierarchical three-species "food chain" model even though species clusters emerge in the system if the system is mixed by pure hopping processes.

Finally, in Chapter 5, through Monte Carlo simulation on a heterogeneous interacting agents model, we investigate the universal scaling phenomena observed in empirical financial markets, such as, long-tail properties of return distribution and trading volume distribution, long-range correlation of volatility, and volatility clustering. In the heterogeneous interacting agents model, all agents/investors are indirectly connected by the listed asset price, which behaves as a global variable and causes the emergence of collective universal scaling behavior in financial markets. Moreover, it is numerically and analytically demonstrated that fat-tail nature of trading volume distribution results in the emergence of power-law tails in the return distributions; and furthermore we find that the fat-tail nature of trading volume distribution is caused by the heterogeneity of degrees of investors' risk-aversion.

6.2 Outlook

We have numerically studied the influence of quenched spatial disorder on the evolutionary dynamics of two-dimensional rock-paper-scissors systems either with or without conservation law, but it remains to be elucidated why the influence of spatial disorder in rock-paper-scissors systems is not so evident as in two-specis Lotka-Volterra model. One method is to employ field-theoretic tools based on the Doi–Peliti representation of the master equation to comprehensively understand the underlying fluctuations and correlations in the spatial three-species cyclic rock-paper-scissors systems. Meanwhile, both numerical simulation and analytic study on the connection between the "corner" May–Leonard model and two-species Lotka-Volterra model are still lacking.

For the heterogeneous interacting agents model shown in Chapter 5, it refers to a finan-

cial market with only one single asset. Therefore, it is worth studying whether the scaling phenomena remain unchanged after considering multiple assets in the market. Moreover, through this interacting agents model, a numerical investigation about the influence of particular trading strategies on the financial market is still lacking. By including additional types of traders (e.g., inside trader, arbitrageur, risk-love trader) into the model, it might become possible to numerically study how the scaling phenomena change when different trading strategy is considered.

Bibliography

[1] R. A. Fisher, *The Genetic Theory of Natural Selection* (Clarendon Press, Oxford, 1930).

[2] Q. He, M. Mobilia and U. C. Täuber, Eur. Phys. J. B **82**, 97-105 (2011).

[3] Q. He, M. Mobilia and U. C. Täuber, *Phys. Rev. E* **82**, 051909 (2010).

[4] Q. He, U. C. Täuber and R. K. P. Zia, e-print arXiv:1111.1674.

[5] R. M. May, *Stability and Complexity in Model Ecosystems* (Cambridge University Press, Cambridge, 1974).

[6] J. Maynard Smith, *Models in Ecology* (Cambridge University Press, Cambridge, 1974).

[7] R. E. Michod, *Darwinian Dynamics* (Princeton University Press, Princeton, 2000).

[8] R. V. Sole and J. Basecompte, *Self-Organization in Complex Ecosystems* (Princeton University Press, Princeton, 2006).

[9] D. Neal, *Introduction to Population Biology* (Cambridge University Press, Cambridge, 2004).

[10] A. J. Lotka, J. Amer. Chem. Soc. **42**, 1595 (1920).

[11] V. Volterra, Mem. Accad. Lincei **2**, 31 (1926).

[12] J. Maynard Smith, *Evolution and the Theory of Games* (Cambridge University Press, Cambridge, 1982).

[13] J. Hofbauer and K. Sigmund, *Evolutionary games and population dynamics* (Cambridge University Press, Cambridge, 1998).

[14] M. A. Nowak, *Evolutionary Dynamics* (Belknap Press, Cambridge(USA), 2006).

[15] G. Szabó and G. Fáth, *Evolutionary games on graphs*, Phys. Rep. **446**, 97 (2007).

[16] D. Volovik, M. Mobilia, and S. Redner, Eur. Phys. Lett. **85**, 48003 (2009).

[17] M. Mobilia, J. Theor. Biol. **264**, 1 (2010).

[18] B. Sinervo and C.M. Lively, Nature **380**, 240 (1996).

[19] K. R. Zamudio and B. Sinervo, Proc. Natl. Acad. Sci. U.S.A. **97**, 14427 (2000).

[20] B. Kerr, M. A. Riley, M. W. Feldman, and B. J. M. Bohannan, Nature **418**, 171 (2002).

[21] J. B. C. Jackson and L. W. Buss, Proc. Nat. Acad. Sci. U.S.A. **72**, 5160 (1975); Am. Nat. **113**, 223 (1979).

[22] L. W. Buss, Proc. Nat. Acad. Sci. U.S.A. **77**, 5355 (1980).

[23] M. T. Burrows and S. J. Hawkins, Mar. Ecol. Prog. Ser. **167**, 1 (1998).

[24] M. Ifti and B. Bergersen, Eur. Phys. J. E **10**, 241 (2003).

[25] T. Reichenbach, M. Mobilia, and E. Frey, Phys. Rev. E. **74**, 051907 (2006).

[26] M. Frean and E. R. Abraham, Proc. R. Soc. Lond. B **268**, 1323 (2001).

[27] M. Berr, T. Reichenbach, M. Schottenloher, and E. Frey, Phys. Rev. Lett. **102**, 048102 (2009).

[28] K. I. Tainaka, J. Phys. Soc. Jpn. **57**, 2588 (1988).

[29] L. Frachebourg, P. L. Krapivsky, and E. Ben-Naim, Phys. Rev. Lett. **77**, 2125 (1996).

[30] L. Frachebourg, P. L. Krapivsky, and E. Ben-Naim, Phys. Rev. E. **54**, 6186 (1996).

[31] A. Provata, G. Nicolis, and F. Baras, J. Chem. Phys. **110**, 8361 (1999).

[32] S. Venkat and M. Pleimling, Phys. Rev. E **81**, 021917 (2010).

[33] K. I. Tainaka, Phys. Lett. A **176**, 303 (1993).

[34] K. I. Tainaka, Phys. Rev. E **50**, 3401 (1994).

[35] G. Szabó and A. Szolnoki, Phys. Rev. E **65**, 036115 (2002).

[36] M. Perc, A. Szolnoki and G. Szabo, Phys. Rev. E **75**, 052102 (2007).

[37] T. Reichenbach, M. Mobilia, and E. Frey, Nature **448**, 1046 (2007).

[38] T. Reichenbach, M. Mobilia, and E. Frey, Phys. Rev. Lett. **99**, 238105 (2007).

[39] T. Reichenbach, M. Mobilia, and E. Frey, *Banach Center Publications* Vol.**80**, 259 (2008).

[40] T. Reichenbach, M. Mobilia, and E. Frey, J. Theor. Biol. **254**, 368 (2008).

[41] G. A. Tsekouras and A. Provata, Phys. Rev. E. **65**, 016204 (2001).

[42] M. Peltomäki and M. Alava, Phys. Rev. E. **78**, 031906 (2008).

[43] S. P. Hubbell, *The Unified Neutral Theory of Biodiversity and Biogeography* (Princeton University Press, Princeton, 2001).

[44] I. A. Hanski and O. E. Gagiotti (Eds.), *Ecology, genetics, and evolution of metapopulations* (Elsevier Academic Press, Burlington, MA, 2004).

[45] A. Dobrienski and E. Frey, e-print `arXiv:1001.5235`.

[46] M. Mobilia, I. T. Georgiev, and U. C. Täuber, J. Stat. Phys. **128**, 447 (2007).

[47] M. J. Washenberger, M. Mobilia, and U. C. Täuber, J. Phys.: Condens. Matter. **19**, 065139 (2007).

[48] U. Dobramysl and U. C. Täuber, Phys. Rev. Lett. **101**, 258102 (2008).

[49] J. D. Murray, *Mathematical Biology Vols. I and II* (Springer-Verlag, New York, 2002).

[50] A. Lipowski and D. Lipowska, *Physica A* **276**, 456 (2000)

[51] A. F. Rozenfeld and E. V. Albano, *Physica (Amsterdam)* **266A**, 322 (1999)

[52] R. Monetti, A. F. Rozenfeld, and E. V. Albano, *Physica A* **283**, 52 (2000).

[53] T. Antal and M. Droz, *Phys. Rev. E* **63**, 056119 (2001).

[54] M. Kowalik, A. Lipowski, and A. L. Ferreira, *Phys. Rev. E* **66**, 066107 (2002).

[55] J. E. Satulovsky and T. Tomé, *Phys. Rev. E* **49**, 5073 (1994)

[56] N. Boccara, O. Roblin and M. Roger, *Phys. Rev. E* **50**, 4531 (1994)

[57] A. Lipowski, *Phys. Rev. E* **60**, 5179 (1999)

[58] D. Panja, *Phys. Rep.* **393**, 87 (2004)

[59] L. O'Malley, B. Kozma, G. Korniss, Z. Rácz, and T. Caraco, *Phys. Rev. E* **74**, 041116 (2006)

[60] S. R. Dunbar, *J. Math. Biol.* **17**, 11 (1983)

[61] J. Sherratt, B. T. Eagen, and M. A. Lewis, *Phil. Trans. R. Soc. Lond. B* **352**, 21 (1997)

[62] M. A. M. de Aguiar, E. M. Rauch, and Y. Bar-Yam, *J. Stat. Phys.* **114**, 1417 (2004)

[63] M. Droz and A. Pekalski, *Phys. Rev. E* **63**, 051909 (2001).

[64] R. K. P. Zia, arXiv: 1101.0018

[65] S. V. Vikram and S. Sinha, *Phys. Rev. E* **83**, 016101 (2011).

[66] E. F. Fama, *Journal of Finance* **25**, 383 (1970).

[67] E. F. Fama and K. R. French, *Journal of Political Economy* **96**, 246-273 (1988).

[68] R. N. Mantegna and H. E. Stanley, *Nature (London)* **376**, 46 (1995).

[69] P. Gopikrishnan, M. Meyer, L. A. N. Amaral and H. E. Stanley, *Eur. Phys. J. B* **3**, 139 (1998); *Phys. Rev. E* **60**, 5305 (1999).

[70] B. B. Mandelbrot, *Journal of Business* **36**, 392 (1963).

[71] T. Lux and M. Marchesi, *Nature* **397**, 498-500 (1999).

[72] V. Belitsky and A. L. Pereira, arXiv:0909.4815

[73] A. Krawiecki, J. A. Holyst and D. Helbing, *Phys. Rev. E* **89**, 5659 (2000).

[74] D. Chowdhury and D. Stauffer, *Eur. Phys. J. B* **8**, 447 (1999); T. Kaizoji, *Physica A* **287**, 493 (2000).

[75] R. M. May and W. J. Leonard, *SIAM J. Appl. Math.* **29**, 243-253 (1975).

[76] R. Durrett and S. Levin, J. Theor. Biol. **185**, 165 (1997); Theor. Pop. Biol. **53**, 30 (1998).

[77] M. Schütt and J.C. Claussen, e-print `arXiv:1003.2427`.

[78] M. Parker and A. Kamenev, Phys. Rev. E **80**, 021129 (2009).

[79] G. Szabó, A. Szolnoki and R. Izsák, *J. Phys. A. Math. Gen.* **37**, 2599 (2004).

[80] A. Szolnoki and G. Szabó, *Phys. Rev. E* **70**, 037102 (2004).

[81] J. C. Claussen and A. Traulsen, *Phys. Rev. Lett.* **100**, 058104 (2008).

[82] H. Touchette, *Phys. Rep.* **478**, 1 (2009).

[83] C. W. Gardiner, *Handbook of Stochastic Methods* (Springer-Verlag, Berlin, 2nd ed., 2002).

[84] U. C. Täuber, *J. Phys.: Conf. Ser.* **319**, 012019 (2011).

[85] V. Alfi, F. Coccetti, M. Marotta, L. Pietronero and M. Takayasu, *Physica A* **370**, 30 (2006); K. Watanabe, H. Takayasu and M. Takayasu, *Phys. Rev. E* **80**, 056110 (2009).

[86] D. M. Guillaume et al., *Fin. Stoch.* **1**, 95-129 (1997).

[87] V. Plerou and H. E. Stanley, *Phys. Rev. E* **76**, 046109 (2007).

[88] J. F. Muzy, J. Delour and E. Bacry, *Eur. Phys. J. B* **17**, 537 (2000); E. Bacry, J. Delour and J. F. Muzy, *Phys. Rev. E* **64**, 026103 (2001).

[89] P. Cizeau, Y. Liu, M. Meyer, C.-K. Peng and H. E. Stanley, *Physica A* **245**, 441 (1997).